The Early Evening Transition in Southeastern U.S. Tornado Environments

MATTHEW C. BROWN,[a] CHRISTOPHER J. NOWOTARSKI,[a] ANDREW R. DEAN,[b] BRYAN T. SMITH,[b] RICHARD L. THOMPSON,[b] AND JOHN M. PETERS[c]

[a] *Department of Atmospheric Sciences, Texas A&M University, College Station, Texas*
[b] *Storm Prediction Center, Norman, Oklahoma*
[c] *Meteorology Department, Naval Postgraduate School, Monterey, California*

(Manuscript received 20 October 2020, in final form 24 May 2021)

ABSTRACT: The response of severe local storms to environmental evolution across the early evening transition (EET) remains a forecasting challenge, particularly within the context of the Southeast U.S. storm climatology, which includes the increased presence of low-CAPE environments and tornadic nonsupercell modes. To disentangle these complex environmental interactions, Southeast severe convective reports spanning 2003–18 are temporally binned relative to local sunset. Sounding-derived data corresponding to each report are used to characterize how the near-storm environment evolves across the EET, and whether these changes influence the mode, frequency, and tornadic likelihood of their associated storms. High-shear, high-CAPE (HSHC) environments are contrasted with high-shear, low-CAPE (HSLC) environments to highlight physical processes governing storm maintenance and tornadogenesis in the absence of large instability. Last, statistical analysis is performed to determine which aspects of the near-storm environment most effectively discriminate between tornadic (or significantly tornadic) and nontornadic storms toward constructing new sounding-derived forecast guidance parameters for multiple modal and environmental combinations. Results indicate that HSLC environments evolve differently than HSHC environments, particularly for nonsupercell (e.g., quasi-linear convective system) modes. These low-CAPE environments sustain higher values of low-level shear and storm-relative helicity (SRH) and destabilize postsunset—potentially compensating for minimal buoyancy. Furthermore, the existence of HSLC storm environments presunset increases the likelihood of nonsupercellular tornadoes postsunset. Existing forecast guidance metrics such as the significant tornado parameter (STP) remain the most skillful predictors of HSHC tornadoes. However, HSLC tornado prediction can be improved by considering variables like precipitable water, downdraft CAPE, and effective inflow base.

SIGNIFICANCE STATEMENT: The environments in which storms occur change near and after sunset, making it difficult to anticipate how these storms will respond and whether they can produce tornadoes. Southeast U.S. tornadoes can occur even with limited instability, which only adds to this challenge. To this end, we examine the different pathways that Southeast storm environments can evolve into the evening and consider how the frequency and characteristics of their tornadoes change for each pathway. We found that the amount of instability present before sunset influences how storm environments change afterward, and, therefore, how those storms produce tornadoes. Last, we identify what variables best predict tornadoes for each pathway, and these are used to construct new Southeast tornado forecasting parameters.

KEYWORDS: Severe storms; Tornadoes; Storm environments; Soundings; Diurnal effects

1. Introduction

The hours soon before and after local sunset constitute the early evening transition (EET), a period during which surface radiational cooling results in increasing static stability and convective inhibition (CIN). These thermodynamic changes are often accompanied by the onset of nocturnal low-level jets (NLLJ; Blackadar 1957; Shapiro et al. 2016), which can introduce additional low-level shear and storm-relative helicity (SRH) into nocturnal storm environments (relative to daytime environments) and have potential ramifications for storm maintenance and tornadogenesis (e.g., Maddox 1993; Markowski et al. 1998; Parker 2014). These and other related factors have been offered up as explanation for the peak in near-sunset tornado counts noted in the literature (e.g., Kelly et al. 1978; Mead and Thompson 2011). Understanding how these environmental features and their impact on accompanying convection evolve with time are vitally important for determining the ability of storms to produce severe hazards through the EET. However, it remains unclear whether presunset thermodynamic and kinematic characteristics influence the nature of this evolution and subsequent storm features.

The impact of boundary layer stabilization on near-ground rotation and the maintenance of intense updrafts has been addressed by the recent literature, largely within the context of supercells (e.g., Ziegler et al. 2010; Nowotarski et al. 2011; MacIntosh and Parker 2017), or transitions between supercells and other convective modes (e.g., Billings and Parker 2012;

Supplemental information related to this paper is available at the Journals Online website: https://doi.org/10.1175/WAF-D-20-0191.s1.

Corresponding author: Matthew C. Brown, matthew_brown@tamu.edu

DOI: 10.1175/WAF-D-20-0191.1

Peters et al. 2017; Geerts et al. 2017; Gropp and Davenport 2018; Gray and Frame 2019). Whether ingesting near-surface (as in MacIntosh and Parker 2017) or elevated air parcels (as in Nowotarski et al. 2011), the updrafts of nocturnal supercells have been shown to persist in spite of increasing environmental near-surface static stability. This resilience may be due to the upward pressure gradient accelerations caused in part by updraft rotation (e.g., Rotunno and Klemp 1982; Rotunno and Klemp 1985), which can lift negatively buoyant air (Markowski et al. 2012). Increases in low-level shear and SRH associated with the NLLJ may enhance upward accelerations in the lower updraft as demonstrated by the results of Coffer and Parker (2015), which act to increase the participation of near-surface parcels within updrafts in spite of their reduced buoyancy, as in Davenport and Parker (2015) and Gray and Frame (2019). These increases in low-level shear (along with deep-layer shear) have also been shown to increase the magnitude of storm-relative (SR) flow (e.g., Warren et al. 2017; Peters et al. 2019), which can both facilitate the transition from nonsupercellular to supercellular modes (Peters et al. 2020b) as well as increase updraft width, buoyancy, and vertical velocity (Peters et al. 2019). Thermodynamic explanations for low-level updraft accelerations have also been offered in studies such as Brown and Nowotarski (2019), which demonstrated that upward buoyancy pressure accelerations (BPA) can exist in supercells below their level of free convection (LFC) despite the presence of CIN and negative buoyancy, which could be of importance for nocturnal supercells. Despite these studies, however, it is not apparent which situations allow these accelerations to overcome low-level stabilization during the EET, and which do not.

Gropp and Davenport (2018) analyzed Great Plains supercells and their near-storm environments as they progress through the EET. Using RUC and RAP proximity soundings, the authors found that large increases in SRH coupled with minimal increases in most unstable (MU)CIN support intense rotating updrafts, allowing supercells to persist well into the evening hours. This agrees with previous studies that found a greater risk of nocturnal supercell tornadoes in the presence of increased SRH (e.g., Davies and Fischer 2009) and reduced low-level static stability (e.g., Mead and Thompson 2011) associated with local moisture increases. This SRH relationship could again be a consequence of increased low-level SR flow (Peters et al. 2019, 2020b). Nevertheless, not all nocturnal tornadoes are supercellular, nor are they confined to the Great Plains. Previous studies of quasi-linear convective systems (QLCS) and their associated hazards (e.g., Trapp et al. 2005; Ashley et al. 2019) as well as the nocturnal tornado climatology of Kis and Straka (2010) have noted a nocturnal maximum in QLCS tornadoes, though the design and precision of their respective QLCS classification methods vary. Such studies specifically noted that Southeast (SE) events comprise an appreciable fraction of the nocturnal and/or QLCS tornado climatologies. These insights, combined with both preexisting and projected vulnerability to SE tornado hazards due to mobile home density, increased poverty rates, population increases, and expanding exurbia footprints (e.g., Simmons and Sutter 2007; Ashley et al. 2008; Strader et al. 2017), have given way to increased research focus on SE U.S. tornadoes.

The aforementioned body of research has noted several characteristics common to SE storms and near-storm environments, including a skew toward cool season months and their nocturnal persistence, characterized by strongly sheared environments with limited buoyancy—termed high-shear, low-CAPE, or HSLC environments (e.g., Guyer and Dean 2010; Sherburn and Parker 2014; Sherburn et al. 2016; Anderson-Frey et al. 2019; Brown and Nowotarski 2020). Even the forcing of relevant atmospheric features like LLJs differ for the Southeast. For instance, Great Plains LLJs are influenced by the region's sloped terrain, whose associated thermal wind reversal in evening hours leads to a geostrophic wind maximum above the surface (e.g., Holton 1967) which can enhance preexisting NLLJs driven by nocturnal decoupling. This sloping terrain influence is diminished in the Southeast, and the strength of LLJs is instead perhaps modulated by ageostrophic jet streak circulations associated with midlatitude cyclones (Uccellini and Johnson 1979). Furthermore, Southeast LLJs and their attendant moisture transport can be enhanced by flow over the Intra-Americas Sea (IAS; Rasmusson 1967). Sometimes referred to as the IAS-LLJ, this feature has been shown to influence precipitation and tornadoes across the Southeast (Muñoz and Enfield 2011).

Regarding predictability, Brown and Nowotarski (2020) demonstrated that climate-scale variability (e.g., Arctic Oscillation) can modulate SE synoptic patterns in ways that make them more favorable for tornado outbreaks, and even contribute to the formation of HSLC environments. On the storm-scale, however, HSLC tornadoes can be more difficult to predict than HSHC tornadoes (Dean and Schneider 2008; Dean and Schneider 2012; Anderson-Frey et al. 2019), and their increased nocturnal frequency poses enhanced risk to the public (e.g., Ashley et al. 2008). These factors provide both scientific and societal impetus to improve our physical understanding of how HSLC storm environments respond to and evolve across the EET, and what consequences these changes have for nocturnal tornadogenesis.

While some of these studies have considered diurnal variation in tornado characteristics, none to our knowledge have specifically examined how the changes in CAPE, shear, SRH, and CIN that occur during the EET influence the characteristics of subsequent tornadoes. One of the few studies we are aware of that has directly addressed the predictability of SE tornadoes occurring in the vicinity of the EET is Bunker et al. (2019), which found that effective-inflow layer quantities are more skillful nocturnal tornado predictors than fixed-layer quantities. The reason for this added skill of effective-inflow layer quantities is unclear, however, as is the matter of whether this skill is retained in low-CAPE environments. In other words, it is possible that the factors that help facilitate tornadogenesis in low-CAPE environments differ from those relevant in high-CAPE environments. Understanding how the atmospheric features discussed thus far evolve in time and in different background environments is crucial to assess the net effect of the EET on tornadogenesis potential. Based on this knowledge gap, this study addresses the following questions:

1) How do CAPE, shear, SRH, and CIN change during the EET in Southeast storm environments, and does this evolution depend on the amount of CAPE present before the EET (e.g., high CAPE versus low CAPE)?
2) If EET evolution is CAPE-dependent, what impact do these differing evolution pathways have on the frequency and storm mode of subsequent tornadoes?
3) What environmental variables best discriminate between SE tornadic (or significantly tornadic) and nontornadic storms, and does their predictive skill vary as a function of background CAPE and/or storm mode?
4) Can existing forecast guidance metrics, such as STP, be adapted to better predict SE tornadoes using these variables?

Using a tornado event database [originally developed by Smith et al. 2012] spanning 2003–18, we seek to identify SE tornadic events spanning the EET and characterize the CAPE and deep-layer shear of their near-storm environments prior to the EET. We will then analyze how these near-storm environments and the characteristics of their attendant convection evolve across the EET as a function of their CAPE and shear classifications. The next section details the severe weather report database and environmental data utilized in this study, as well the rationale for case selection and temporal binning. Section 3 reports on the results of our analyses, including the temporal characteristics of the SE tornado climatology, the evolution of the near-storm environment and associated storm and tornado characteristics, and the predictability of these tornadoes using proximity sounding–derived quantities. Finally, section 4 discusses the implications of these findings within the broader scope of the literature, as well as future research directions relevant to the study at hand.

2. Data and methods

The storm reports utilized in this study are from the updated version of the dataset originally developed in Smith et al. (2012), as used in Anderson-Frey et al. (2019), appended with all 2018 events. This tornado event dataset is developed by mapping county tornado segment data onto a $40 \times 40\ \text{km}^2$ grid, and filtering such that the highest (E)F-scale rating is retained in every given hour and grid box. Severe wind or hail reports corresponding to grid hours with no tornadoes are used to characterize nontornadic environments.[1] Environmental data are matched with each report using the closest data grid point from the SPC hourly mesoanalysis grids (Bothwell et al. 2002), the basis of which are the Rapid Update Cycle (RUC; Benjamin et al. 2004) or Rapid Refresh Model (RAP; Benjamin et al. 2016), using the same 40-km grid spacing as the grid-hour report filtering described previously. Furthermore, the models assimilate rawinsonde, profiler, radar, lightning, and other data (Benjamin et al. 2016, their Table 3). Profiles of temperature, moisture, and wind above the ground were based on the RUC model through April 2012, and the RAP model beginning in May 2012, with data every 25 hPa in the vertical. The SHARPpy sounding analysis software (Blumberg et al. 2017) was used for all parameter calculations for the SPC mesoanalysis sounding profiles matched to each grid-hour tornado or severe-storm event. As with any model output, this dataset carries its own limitations and biases, the details of which are discussed extensively in Thompson et al. (2012) and Anderson-Frey et al. (2016). Limitations relevant to this study—particularly grid spacing—are discussed in later sections.

Radar data and a convective mode decision tree (Fig. 2 in Smith et al. 2012) are then used to manually classify convective mode. As noted in previous literature, the majority of resulting modes such as QLCS and right-moving supercell (RMS) are mutually exclusive, though some overlap is allowed with classifications such as tropical cyclone (TC). Similar to Brown and Nowotarski (2020), all reports associated with TCs are removed, as TC tornado environments are beyond the scope of this study. The remaining storm modes are consolidated into three broad categories—supercell (including all isolated supercells and supercell in line features), QLCS (including all QLCS, bow echo, and nonsupercellular cell in line structures), and disorganized (all nonsupercellular clusters, cells, and any combinations thereof). Additionally, tornadoes with rating F/EF0–1 are considered weakly tornadic, and F/EF2+ considered significantly tornadic.[2] The same domain defined in Anderson-Frey et al. (2019), consisting of Alabama, Arkansas, Georgia, Kentucky, Louisiana, Mississippi, and Tennessee, is used for consistency with previous literature.

To isolate storm environments likely impacted by the EET, local sunset (SS) time is computed for each storm report based on its location and time of year, and rounded to the nearest hour. Each storm report time is similarly rounded, and then arranged into hourly bins relative to its associated SS. The EET is defined following past studies of this time of day, such as Anderson-Frey et al. (2019), spanning ±2 h off local SS time. The four hours immediately prior to and after this transition (i.e., from SS − 6 to SS − 3, and from SS + 3 to SS + 6) constitute the pre- and post-transition periods, respectively. By focusing our analyses on this ±6-h window centered on local SS, we can specifically analyze the environmental changes introduced by the EET, and limit potential overlap of severe convection persisting into subsequent days.

We also seek to classify background CAPE/shear to assess potential influence on environmental changes across the EET. Numerous classification methods have been implemented in the literature. For the purposes of this study, we have chosen a

[1] Significant wind and hail reports are obtained using conventional definitions for 2003–12. Wind and hail reports from 2014 to 2015 were obtained as part of Thompson et al. (2017), which employs an additional effective bulk shear criterion of 40 kt (1 kt ≈ $0.51\ \text{m s}^{-1}$). Nontornadic cases are not included for 2013 and 2016–18. Analyses were recomputed for only 2003–12 reports to test sensitivity to these varying classifications, and results largely remained unchanged.

[2] These cutoffs are chosen for consistency with numerous other studies in the literature. The suitability of these cutoffs for the SE tornado climatology is examined in section 4.

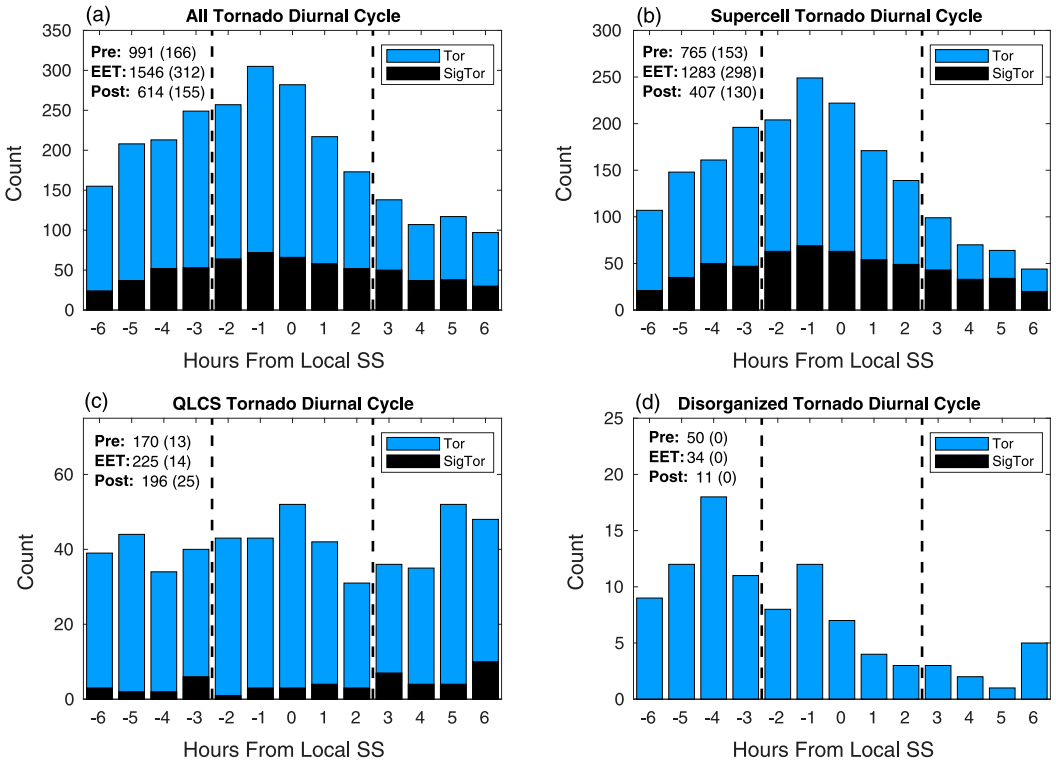

FIG. 1. Diurnal cycle of tornadoes (in light blue) and sigtors (in black) during the pre-transition, EET, and post-transition for (a) all, (b) supercell, (c) QLCS, and (d) disorganized tornadoes, with the EET bounds delineated by black dotted lines; the number of tornadoes in each period is shown in the top left with and number of sigtors in parentheses.

blend of two common methods in which a 0–6-km bulk wind difference (SHR6) of $\geq 18\,\mathrm{m\,s^{-1}}$ is used to denote high-shear. Low-shear conditions are not examined as they correspond to only 10% of all SE tornadoes, consistent with the SHR6 distributions of Thompson et al. (2013). Low-CAPE is defined as an environment with surface-based (SB)CAPE $\leq 500\,\mathrm{J\,kg^{-1}}$ as well as MUCAPE $\leq 1000\,\mathrm{J\,kg^{-1}}$ (as in Sherburn and Parker 2014), while high-CAPE requires mixed-layer (ML)CAPE $\geq 1000\,\mathrm{J\,kg^{-1}}$ (e.g., the complement of the method used in Anderson-Frey et al. 2019). This approach gives two mutually exclusive CAPE/shear categories (HSHC and HSLC) and will assist in determining how aspects of the near-storm environment relevant to tornadogenesis change as a function of buoyancy.

3. Results

a. Diurnal tornado distributions

The criteria described above yield 9250 severe events spanning 1448 individual days (1200–1200 UTC periods) in our prescribed domain and study period. Limiting our scope to the three periods defined earlier (pre-transition, EET, and post-transition), there are 7052 severe events spanning 1258 unique EET periods (±6 h from local SS). Of these reports, 2796 (39.6%) are significant wind (sigwind), 1105 (15.7%) are significant hail (sighail), 2518 (35.7%) are weak tornadoes (weaktor), and 633 (9.0%) are significant tornadoes (sigtor). These 3151 tornadoes represent over 70% of all SE tornado reports, further underscoring the need to understand the environmental changes induced during the EET.

Before we consider environmental evolution, however, we must examine the temporal distribution of SE tornadoes. Figure 1a shows the diurnal cycle of SE tornadoes (in light blue) and sigtors (in black) during the pre-transition, EET, and post-transition periods (marked in dotted black). Tornadoes show a broad bell curve skewed slightly toward pre-SS hours, peaking one hour prior to sunset. Sigtors peak at this same hour, but show less diurnal variability overall such that sigtors account for a larger fraction (over 25%) of post-transition tornadoes. Figures 1b–d break down these diurnal tornado distributions further by mode. Unsurprisingly, we see that supercell tornadoes and sigtors (Fig. 1b)—the predominant tornadic mode in the climatology—are nearly identical to the overall distribution, though sigtors make up an even larger fraction of nocturnal supercell tornadoes. QLCS tor/sigtors (Fig. 1c) are less frequent than supercell tornadoes, but still constitute an appreciable fraction of the SE tornado climatology. This QLCS subset exhibits almost no diurnal variation, with tornadoes and sigtors occurring somewhat equally through the EET. Disorganized tornadoes (Fig. 1d) differ entirely in that they are largely confined to daytime hours and contain no sigtors, as might be expected for this convective

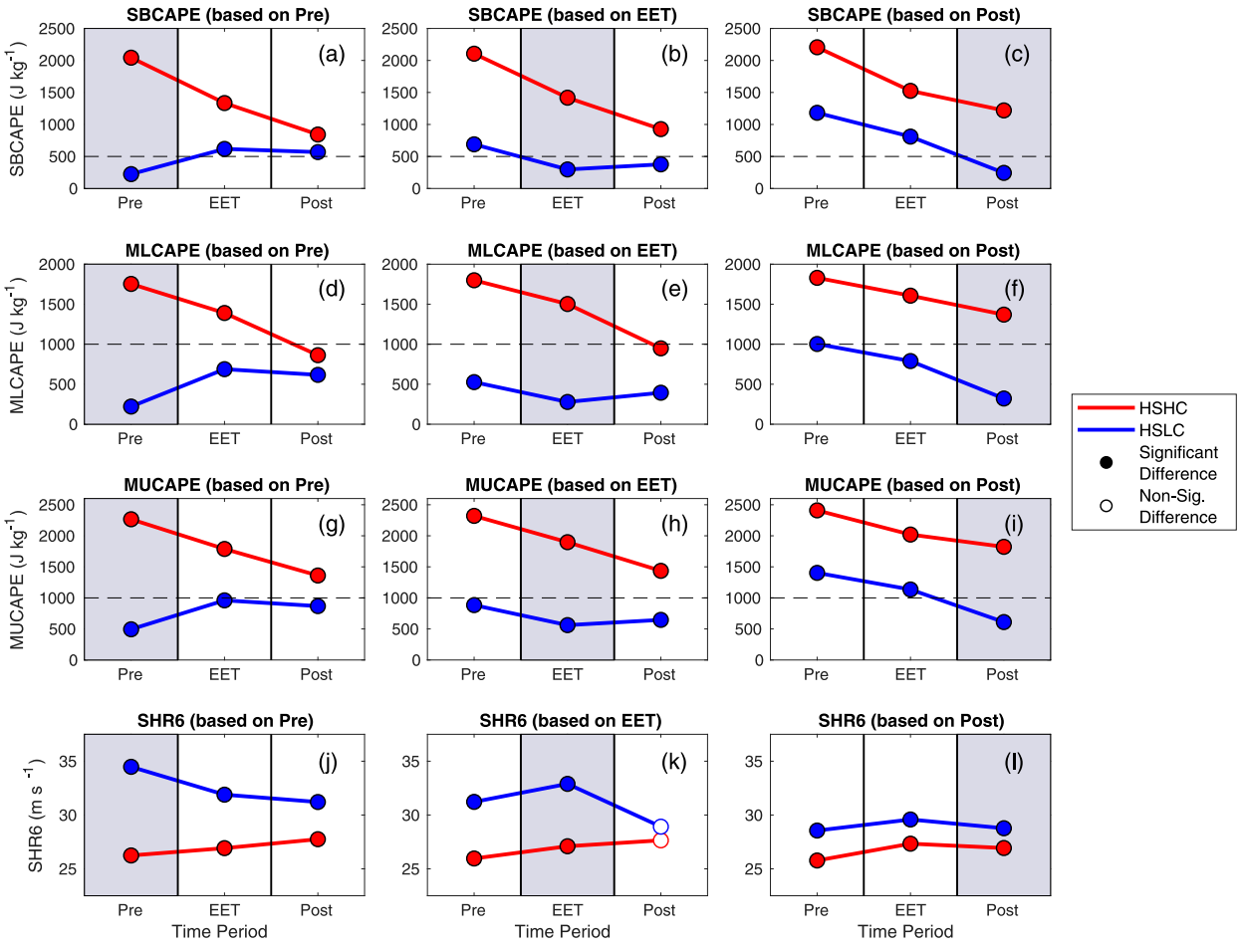

FIG. 2. Time series of average (a)–(c) SBCAPE ($J\,kg^{-1}$), (d)–(f) MLCAPE ($J\,kg^{-1}$), (g)–(i) MUCAPE ($J\,kg^{-1}$), and (j)–(l) 0–6-km shear ($m\,s^{-1}$) based on environment in the pre-transition (Pre, column 1), early evening transition (EET, column 2), and post-transition (Post, column 3). Gray shading corresponds with the period on which each pattern is predicated, and red and blue lines correspond to HSHC and HSLC environmental classifications, respectively; black dotted lines mark thresholds corresponding to our CAPE classification scheme. Filled (unfilled) data points represent statistically significant (insignificant) differences between HSHC and HSLC patterns in each period, following two-sample *t* tests (at the 95% confidence level).

mode. Post-EET increases in nonsupercellular tornado counts may be related to the theorized peak in NLLJ intensity roughly 6-h postsunset presented in the literature (Shapiro et al. 2016), though this model applies to the Great Plains NLLJ.

b. Storm environment evolution

The near-storm environment can change quickly and substantially during the EET. For instance, afternoon HSHC conditions may transition to evening HSLC conditions as buoyancy decreases in response to EET cooling and stabilization. Therefore, we must examine these changes and determine whether they have an impact on the frequency, timing, and convective mode of tornadoes. To do so, we categorize each severe convective day based on when its associated storm reports occurred; these temporal groupings include the pre-transition, EET, and post-transition (as defined earlier) and all combinations thereof, resulting in seven mutually exclusive categories. The category of days with reports in only the pre- and post-transition periods is excluded from subsequent analyses due to substantially smaller report counts. By analyzing the remaining categories, we can ascertain what aspects of the near-storm environment impede or facilitate the maintenance of severe convection across the EET.

We will first examine the days in which storms persisted across all three of our defined periods. Interestingly, only 10% of severe convective days in the SE climatology fall in this category, emphasizing the unique conditions that are likely necessary for convection to produce severe hazards through the EET. For each day and period, we classify its general CAPE/shear characteristics and consider how variables evolve consequently. For instance, if the average pre-transition environment is HSHC, how do CAPE and shear evolve consequently? Alternatively, if the post-transition environment is HSHC, how do CAPE and shear evolve earlier to arrive at that environment? This process is carried out for both environmental classifications, providing a "road map" of how storm

TABLE 1. Storm report count for days with severe convection across all three temporal periods, broken down by environmental classification; total counts are provided along with counts attributed to supercell (SC) and QLCS modes.

Storm environment (period)	No. of Pre-reports [All (SC/QLCS)]	No. of EET reports [All (SC/QLCS)]	No. of Post-reports [All (SC/QLCS)]
HSHC (Pre)	423 (311/80)	872 (515/258)	353 (136/190)
HSHC (EET)	344 (246/71)	754 (453/225)	313 (134/152)
HSHC (Post)	219 (184/15)	379 (261/81)	185 (86/86)
HSLC (Pre)	43 (10/32)	109 (54/43)	34 (11/22)
HSLC (EET)	83 (37/42)	168 (87/71)	108 (30/68)
HSLC (Post)	220 (124/81)	555 (331/160)	203 (54/127)

environments can evolve diurnally, as shown in Fig. 2. Each figure column corresponds to the period that is being used to determine the CAPE/shear category (i.e., column 1 graphs are classified based on the pre-transition environment, and so on as shaded in gray). HSHC and HSLC patterns are displayed in red and blue, respectively. This means, for example, that a blue line in column 2 represents a pattern corresponding to days in which the EET has average HSLC conditions. A two-sample *t* test (at the 95% confidence level) is carried out between the data in each period. Filled (unfilled) data points indicate when the differences between the HSHC and HSLC patterns are statistically significant (insignificant). The sample sizes associated with these patterns are provided in Table 1.

HSHC environments show gradual decreases in CAPE throughout the day regardless of which period is used. HSLC CAPE patterns, however, vary based on the constraining period. When the pre-transition environment is HSLC (blue line in column 1), CAPE values start low, but increase gradually during the EET, likely due to increases in moist instability signaled by changes in low-level equivalent potential temperature θ_e (as computed in SHARPpy; supplemental Fig. 1a) or other related low-level thermodynamic variables (supplemental Table 1). When the EET or post-transition environment is HSLC (blue line in columns 2–3, respectively), CAPE starts at moderate values during the pre-transition, before decreasing and remaining relatively low. Interestingly, HSLC CAPE values remain statistically lower than HSHC values the entire day, despite being conditioned on only one period. Regarding SHR6, both environments exhibit sustained, high values the entire day regardless of the constraining period, but HSLC patterns (particularly those based on the pre-transition and EET) maintain higher overall shear magnitudes than HSHC. If we were to examine those environments that comprise the middle ground between these classifications (high shear, moderate CAPE), we would see that their associated CAPE/shear values understandably lie in between the HSHC and HSLC patterns, but the shape of their patterns largely resemble HSHC patterns.

If we consider the implications of these patterns for storm environment, we see that HSHC environments remain almost entirely in that environmental category, despite diurnal CAPE decreases. In contrast, there are no mean pathways in which an HSLC storm environment persists from the pre-transition through to the post-transition. Rather, HSLC environments on average are transient, evolving from or into other environments throughout the day (even all the way from HSHC conditions). In fact, only four severe convective days in the entire dataset maintain average HSLC conditions through all three periods. This of course could be influenced by the coarse spatial resolution of the environmental dataset utilized and the CAPE/shear thresholds employed, the implications of which are discussed later. However, these insights, combined with the fact that these HSLC transitions occur primarily near local SS, highlight the unique relationship between the EET and the formation of HSLC environments.

To characterize the low-level accelerations potentially associated with the NLLJ, Fig. 3 displays 0–1-km SRH and shear patterns (SRH1 and SHR1, respectively) following the same approach as Fig. 2. As is expected, both of these quantities show relatively similar patterns, with SRH1/SHR1 values steadily increasing through and past local SS. As with SHR6, HSLC pre-transition and EET conditions correspond to uniformly higher SRH1/SHR1 values than HSHC patterns. Though representing a different portion of the atmosphere, effective layer SRH (Eff SRH) was also considered, and showed similarly favorable SRH trends associated with HSLC pre-transition conditions (supplemental Fig. 2a). Interestingly, HSLC pre-transition patterns show a decrease in SRH1/SHR1 during the EET before rapid post-transition increases, perhaps related to changes in boundary layer mixing and/or stabilization. Regardless, these observations suggest that at least some portion of these storm environments coincide with the strengthening flow and helicity associated with an intensifying LLJ, which may play a compensating role in buoyancy-deficient environments.

Given studies such as Mead and Thompson (2011) and Gropp and Davenport (2018) relating CIN to nocturnal supercell maintenance, Fig. 4 shows time series of SB, ML, and MUCIN following the same environment-time classification of Fig. 2. Regardless of the period used for classification, HSHC CIN values generally increase in absolute magnitude with time. The same can be said of several HSLC CIN patterns, particularly those conditioned on the post-transition environment (column 3 in Fig. 4). Though these patterns are largely indistinct from HSHC post patterns, uniformly lower downdraft CAPE (DCAPE) values (supplemental Fig. 3c) may contribute to weaker (e.g., less negatively buoyant) outflow such that storm updrafts are able to persist despite lower CAPE and increasing CIN. In contrast to these HSLC Post patterns, CIN patterns associated with pre-transition or EET HSLC conditions (Figs. 4a,b,e,h) exhibit *destabilization* (or more gradual stabilization) as the evening progresses, with statistically

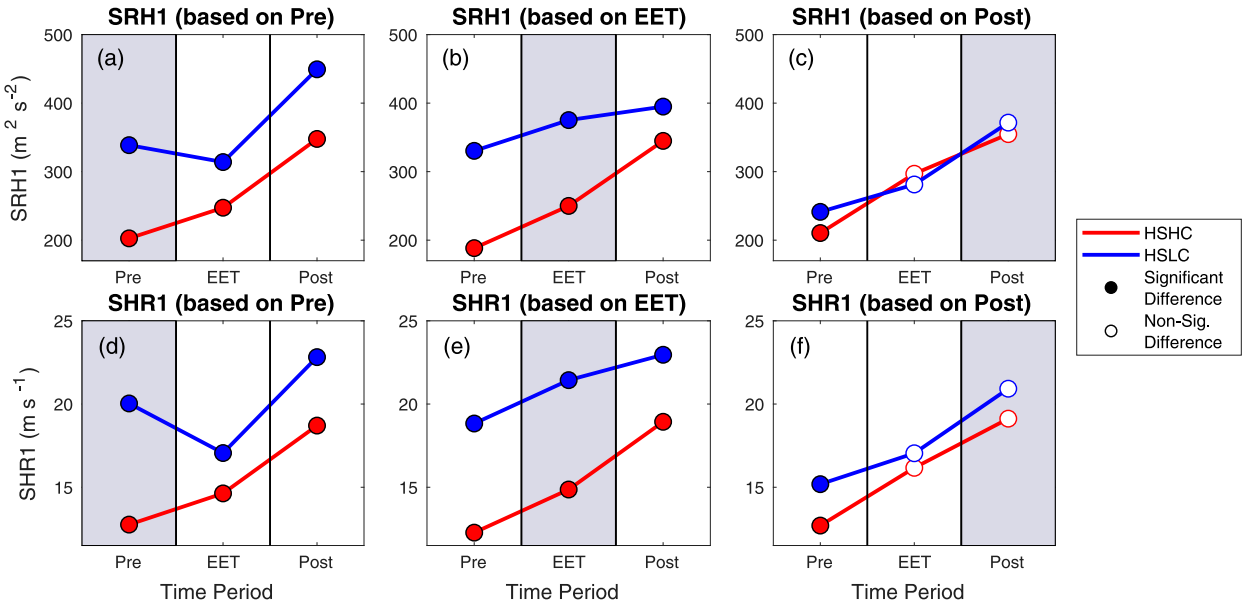

FIG. 3. Time series of average (a)–(c) SRH1 ($m^2 s^{-2}$) and (d)–(f) SHR1 ($m s^{-1}$), with the same line/color scheme as in Fig. 2.

smaller nighttime CIN magnitudes relative to HSHC patterns. These decreases in CIN magnitude develop in tandem with increases in low-level lapse rates (supplemental Fig. 1b), presumably driven by warm-air advection (or differential advection) often associated with NLLJs.

Clearly the near-storm environments of SE storms evolve differently as a function of CAPE/shear characteristics, so it should stand to reason that the frequency and convective modes of their tornadoes do so too. To test this, we consider both the fraction of storm reports in each period that are tornadic, as well as the modal breakdown of those tornadoes, following the same period classification as Figs. 2–4. Normalizing by climatological fractions in each period,[3] we diagnose the percentage change in the frequency and mode of tornadoes, as shown in Fig. 5. For instance, if climatologically 5% of all reports in the pre-transition produce tornadoes, and some subset of those reports associated with one of our environmental classifications is comprised of 7.5% tornadoes, Fig. 5 would display a 50% increase in the fraction of pre-transition storms (for that classification) that produce tornadoes.

Interestingly, HSHC conditions have a limited influence on tornado fraction, though HSHC post-transition conditions (red bars in Fig. 5c) correspond to slightly increased EET and post-transition tornado fractions likely due to overall higher CAPE values. HSLC conditions in a given period lead to decreases in tornado fraction *during that period* (i.e., pre-transition HSLC bar in Fig. 5a, post-transition HSLC bar in Fig. 5c), likely due to their inherently limited instability. However, pre-transition HSLC conditions progress with large pre to post-transition swing toward increased tornado fraction in association with overall higher and increasing SRH1/SHR1 values (Figs. 3a,d) and postsunset decrease in SBCIN magnitude (Fig. 4a). If we condition based on the high-shear, moderate-CAPE environment discussed earlier (not shown), we see large, uniform increases in tornado (and sigtor) fraction regardless of the threshold period, which could imply there exists an ideal combination of the ample instability of HSHC environments and invigorated low-level dynamic support of HSLC environments.

Regarding mode, HSHC conditions tend to have a small, but generally positive effect on the prevalence of supercellular tornadoes, particularly when the post-transition has HSHC conditions (Fig. 5f). HSLC conditions in any period, as with tornado fraction, facilitate a decrease in supercellular tornadoes in that and subsequent periods (Figs. 5d–f). Conversely, these HSLC conditions correspond to an increase in the prevalence of QLCS tornadoes (Figs. 5g–i). If we were to consider raw changes relative to climatology (not shown) rather than normalized changes, we would see that these shifts in the prevalence of supercell and QLCS tornadoes are nearly equal and opposite, implying a direct trade-off between these modes as a function of environment. It is worth noting that the relative magnitudes of the HSHC and HSLC trends may be influenced by differing sample sizes (also shown in Table 1), but these results still highlight the noticeable influence that the daytime storm environment can have on storm characteristics later that evening.

Given the modal exchanges shown in Fig. 5d-i, Figs. 6–8 present the patterns of Figs. 2–4, respectively, separated by mode. Given reduced sample size in portions of this modal subset, median values and Mann–Whitney tests are substituted for mean values and *t* tests in order to account for potential nonnormality. Solid lines represent supercell patterns and dashed represent QLCS patterns, and statistical testing is performed across environments for each mode (e.g., data

[3] These climatological fractions were computed across all days in which convection persisted across all three periods.

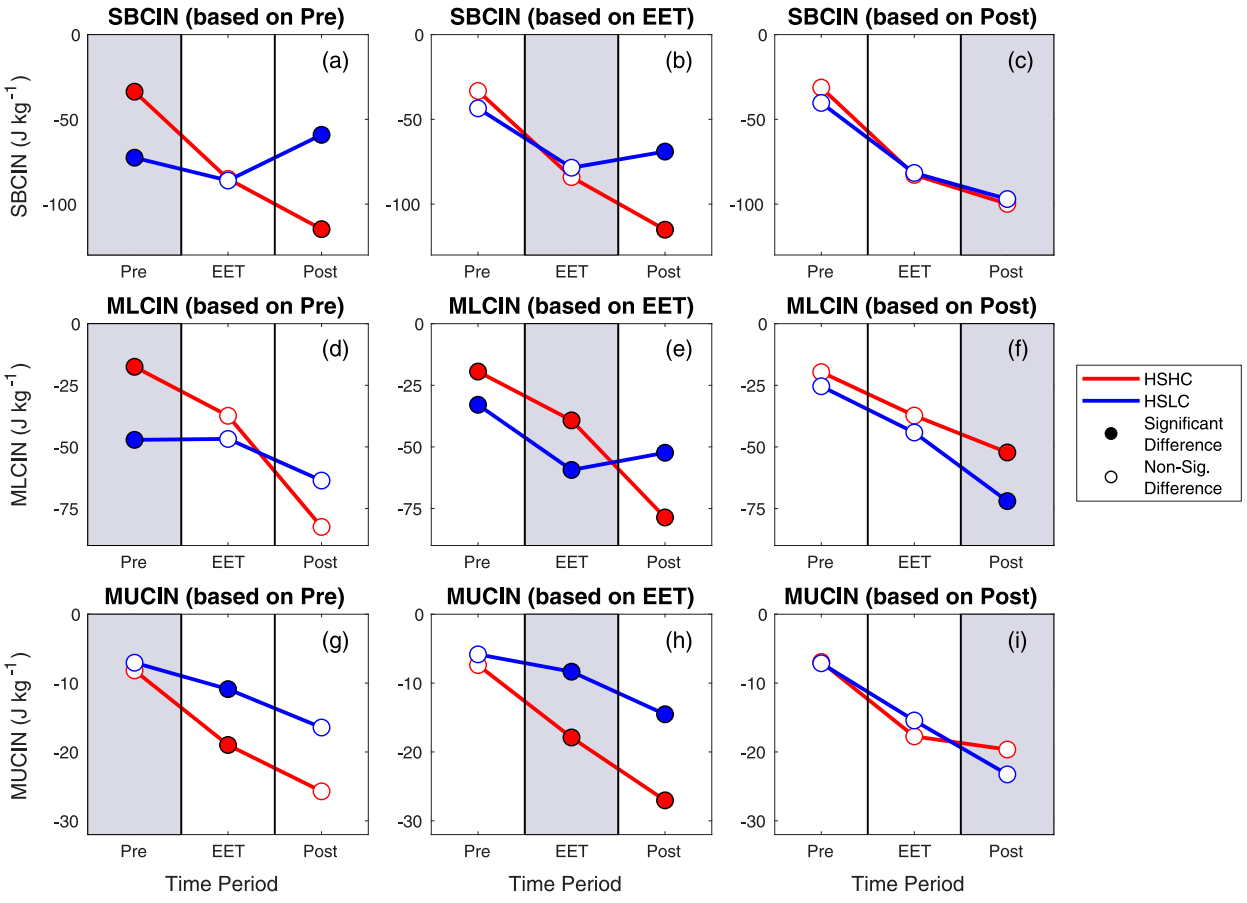

FIG. 4. Time series of average (a)–(c) SBCIN, (d)–(f) MLCIN, and (g)–(i) MUCIN (all in J kg^{-1}), with the same line/color scheme as in Fig. 2.

points on dotted lines represent statistical differences between HSHC and HSLC QLCS patterns). Figures 6a–i shows that CAPE patterns are generally consistent across mode, with slightly higher CAPE values for supercells. The same can be said of SHR6 (Figs. 6j–l), though the differences between HSHC and HSLC QLCS patterns are more pronounced than they are for supercells. This latter point is also true for SRH1/SHR1 (Fig. 7), particularly when conditioning on the pre-transition environment (Figs. 7a,d). Also peculiar in Fig. 7a is that the HSLC Pre pattern associated with supercells does *not* show the monotonic SRH1/SHR1 increase that the QLCS pattern does, suggesting diminished NLLJ influence and perhaps more influence of cyclone-induced LLJs (as with the strong synoptically forced HSLC environments in Sherburn et al. 2016). The HSLC nocturnal destabilization demonstrated in Fig. 4 is also apparent in the modal CIN patterns of Fig. 8, though post-transition CIN values are smaller in magnitude for supercells. Altogether, these modal patterns suggest that increased low-level shear/SRH associated with HSLC conditions can be primarily attributed to QLCS modes, which draws into question what environmental factors are compensating for a lack of instability in HSLC supercell environments. Perhaps the subtle destabilization shown in Figs. 6, 8 coupled with overall high shear values is sufficient to sustain supercells in HSLC Pre environments.

As noted, however, it is far more likely for severe convection *not* to persist through all three periods. Thus, we also consider the evolution of environmental variables as a function of nocturnal persistence. For instance, do variables like CAPE evolve differently for storms occurring only in the pre-transition relative to those which persist into subsequent periods? Figure 9 shows the hourly averaged variables examined in Figs. 2–4 along with three derived parameters associated with each temporal period combination. The sample sizes for each temporal category (summed over each of its constituent periods) are included in Table 2. The limiting factor for storms to persist past that pre-transition appears to be overall smaller values of SRH/SHR variables, as with storms occurring solely in the pre-transition period (red lines in Figs. 9d–f). Though convection clearly can form in these environments, the favorable dynamic forcing associated with increased shear and SRH may be necessary for storms to survive the rapid CAPE decreases and CIN magnitude increases of the EET. The same can be said about storms that fail to persist past the EET (orange and yellow lines in Figs. 9d–f), which have noticeably lower EET SRH1/SHR1 values compared to patterns which persist into the post-transition (green and black lines in Figs. 9d–f). These EET-limited patterns also display more rapid decreases in MLCAPE and increases in MUCIN

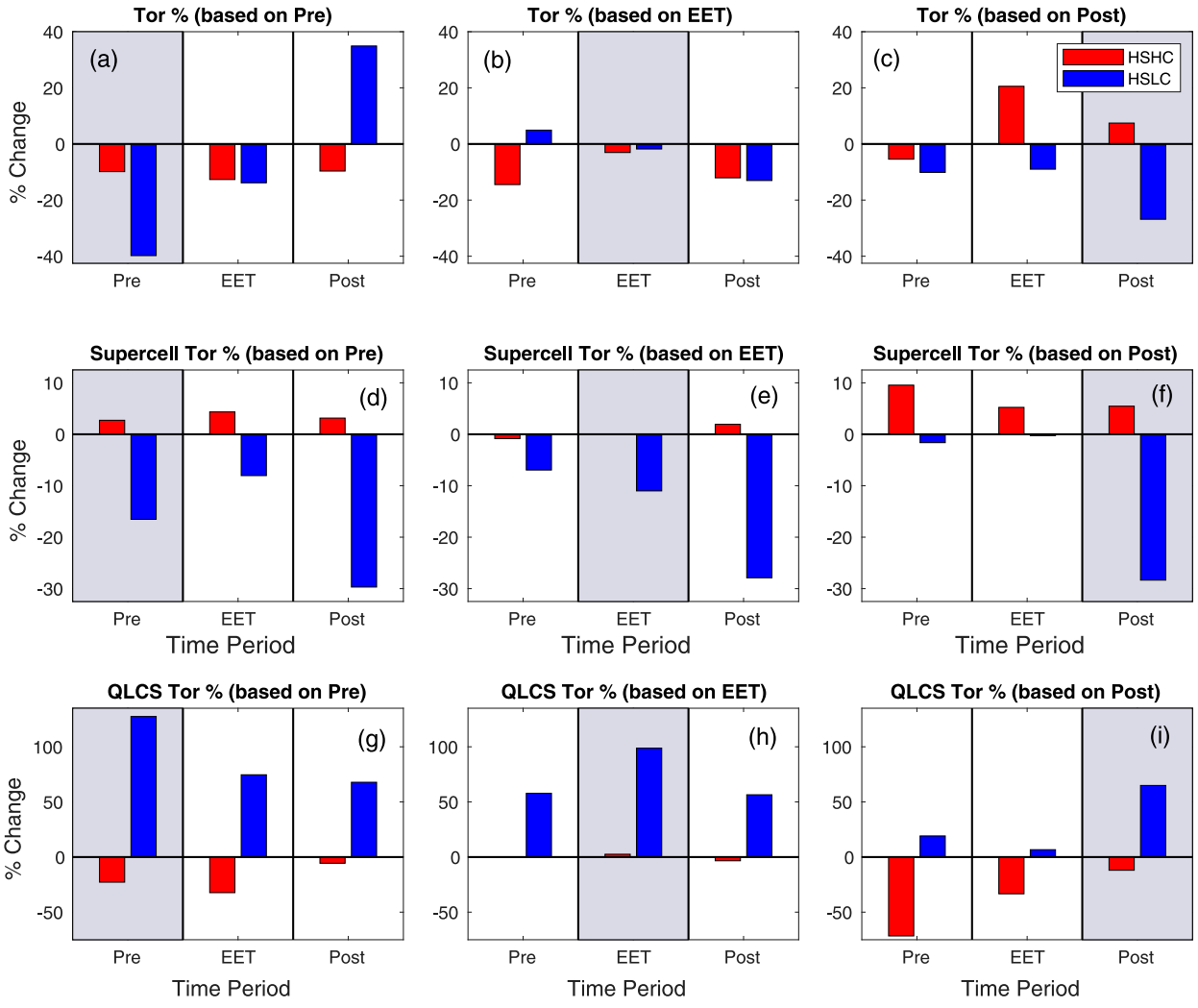

FIG. 5. Bar plots displaying the percent change (relative to climatological average fraction in each period) of (a)–(c) fraction of storms producing tornadoes and the fraction of those tornadoes occurring within (d)–(f) supercells and (g)–(i) QLCS modes, with the same time classification and color scheme as in Fig. 2.

magnitude (Figs. 9b,i, respectively). Conversely, days in which convection spans all three periods (black lines) exhibit sustained higher values of shear and SRH paired with more gradual changes in CAPE and CIN. These differences manifest themselves in the evolution of common derived metrics, including supercell composite parameter (SCP; Thompson et al. 2012), the original STP formulation (STP-T03; Thompson et al. 2003) and effective layer STP (STP-E; Thompson et al. 2012), as shown in Figs. 9j–l. Of the derived metrics utilized in this study (as summarized later), STP-T03 shows the largest spread numerically between the different temporal periods for STP parameters, as does SCP for non-STP parameters.

We then ask whether the environmental variability in Fig. 9 influences the prevalence and characteristics of tornadoes among the analyzed temporal categories. To this end, Fig. 10 shows the period-wide tornado characteristics for the storms contributing to the patterns in Fig. 9, following the same color scheme. These include the fraction of all storms in each period (as indicated in Table 2) producing tornadoes (Fig. 10a) and sigtors (Fig. 10b), as well as the convective mode (Figs. 10c–d) and environment (Figs. 10e–f) of these tornadoes. This means, for example, that the yellow circle in Fig. 10a corresponds to the fraction of storms contributing to the yellow lines in Fig. 9 that produced a tornado. From Figs. 10a–b, we see that the highest tor and sigtor percentages occur in those categories involving the EET and/or the post-transition, possibly related to overall higher 0–1-km shear and SRH values maintained on these days. For storm mode (Figs. 10c–d), the majority of tornadoes occur in supercells, regardless of category or period. Regarding environment, Fig. 10e shows that the two categories spanning both the EET and post-transition (EET and Post, and All Periods) have noticeably higher HSHC fractions, consistent with the CAPE patterns presented thus far. Additionally, the prevalence of HSLC tornadoes gradually increases as the day progresses (Fig. 10f), along with an increase in QLCS tornado percentage, as suggested by the tornado diurnal cycles

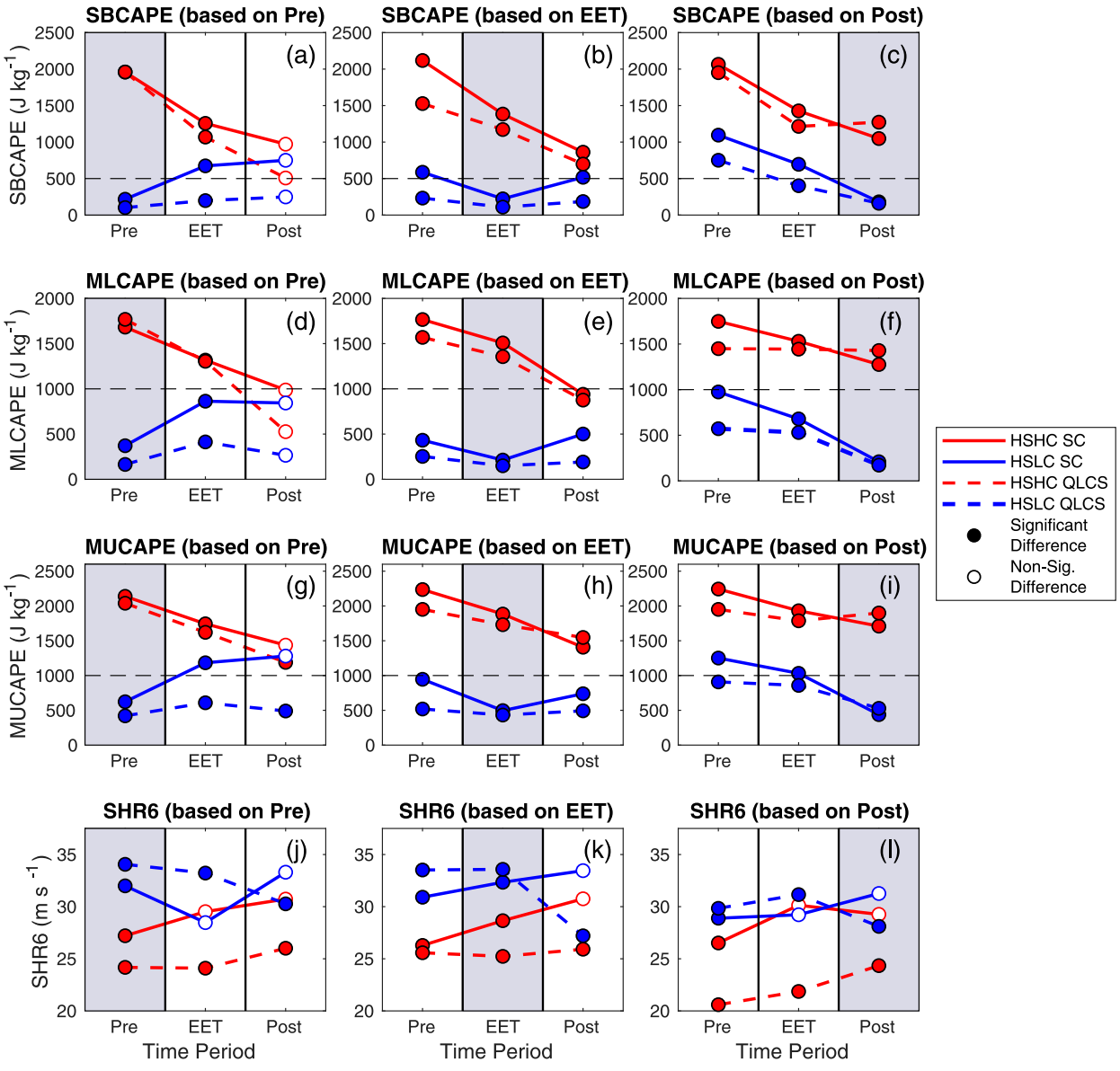

FIG. 6. Time series of median (a)–(c) SBCAPE (J kg^{-1}), (d)–(f) MLCAPE (J kg^{-1}), (g)–(i) MUCAPE (J kg^{-1}), and (j)–(l) 0–6-km shear (m s^{-1}), with the same time classification and color scheme as in Fig. 2, but now broken down by convective mode (solid lines for supercell, or SC, patterns and dotted lines for QLCS patterns). Filled (unfilled) data points represent statistically significant (insignificant) differences between modal HSHC and HSLC patterns in each period, following Mann–Whitney *U* tests (at the 95% confidence level).

in Fig. 1. The same general trends hold true for sigtors (not shown), though understandably an increased skew toward HSHC and supercell classifications exist for this subset of tornadoes.

c. *Storm environment and tornado predictability*

The factors contributing to tornadogenesis in high-CAPE (particularly HSHC) environments have been thoroughly explored in the literature, but less in low-CAPE environments. As such, we seek to identify environmental variables that effectively discriminate between tornadic (or significantly tornadic) and nontornadic storms in HSLC environments and compare them to HSHC predictors. There are a number of potential physical pathways by which HSLC environments may be able to sustain robust low-level updrafts and support tornadogenesis. From a thermodynamic perspective, previous HSLC studies (e.g., Sherburn and Parker 2014; Sherburn et al. 2016) have demonstrated that increased low-level (e.g., 0–1, 0–3 km) lapse rates help sustain HSLC convection by invigorating low-level buoyant accelerations, and therefore contribute to their longevity and ability to develop intense near-surface vortices (Sherburn and Parker 2019). Similar consequences may result from an accumulation of low-level instability such as 0–3-km CAPE (Sherburn et al. 2016), or less negatively buoyant outflow (e.g., Markowski et al. 2002;

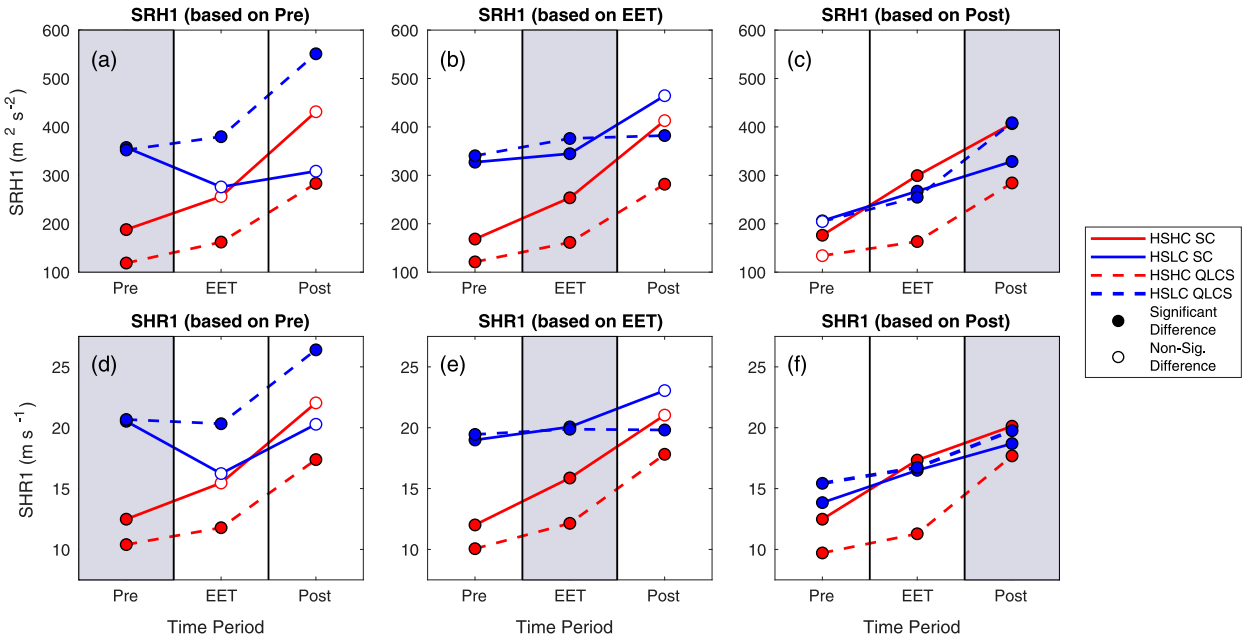

FIG. 7. Time series of median (a)–(c) SRH1 ($m^2 s^{-2}$) and (d)–(f) SHR1 ($m s^{-1}$), with the same line/color scheme as in Fig. 6.

Shabbott and Markowski 2006; Brown and Nowotarski 2019). Alternatively, increased low-level shear and SRH in the presence of a low-level mesocyclone can result in dynamically enhanced vertical accelerations (e.g., Coffer and Parker 2015; Sherburn and Parker 2019), which dominate the production of intense low-level vertical velocities in CAPE-deficient storms (Wade and Parker 2021). Also relevant for low-level updraft maintenance are the storm's effective inflow layer (EIL)

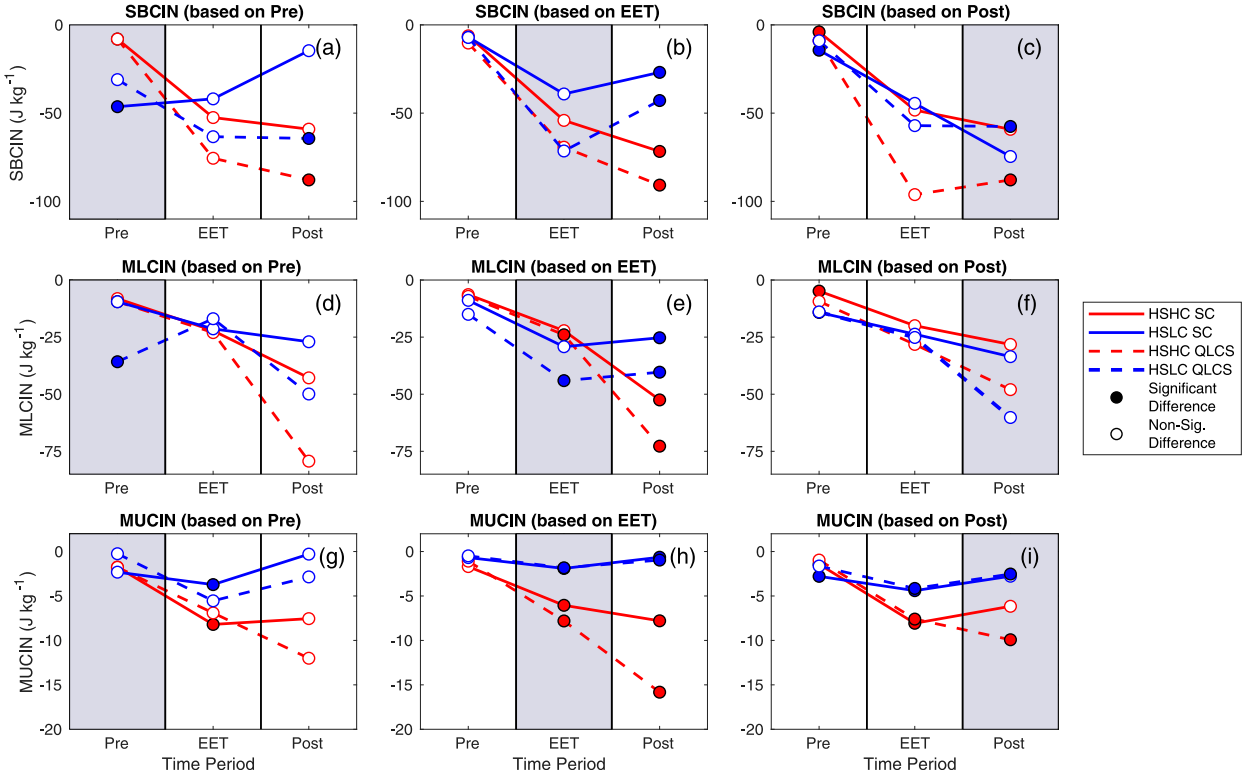

FIG. 8. Time series of median (a)–(c) SBCIN, (d)–(f) MLCIN, and (g)–(i) MUCIN (all in $J kg^{-1}$), with the same line/color scheme as in Fig. 6.

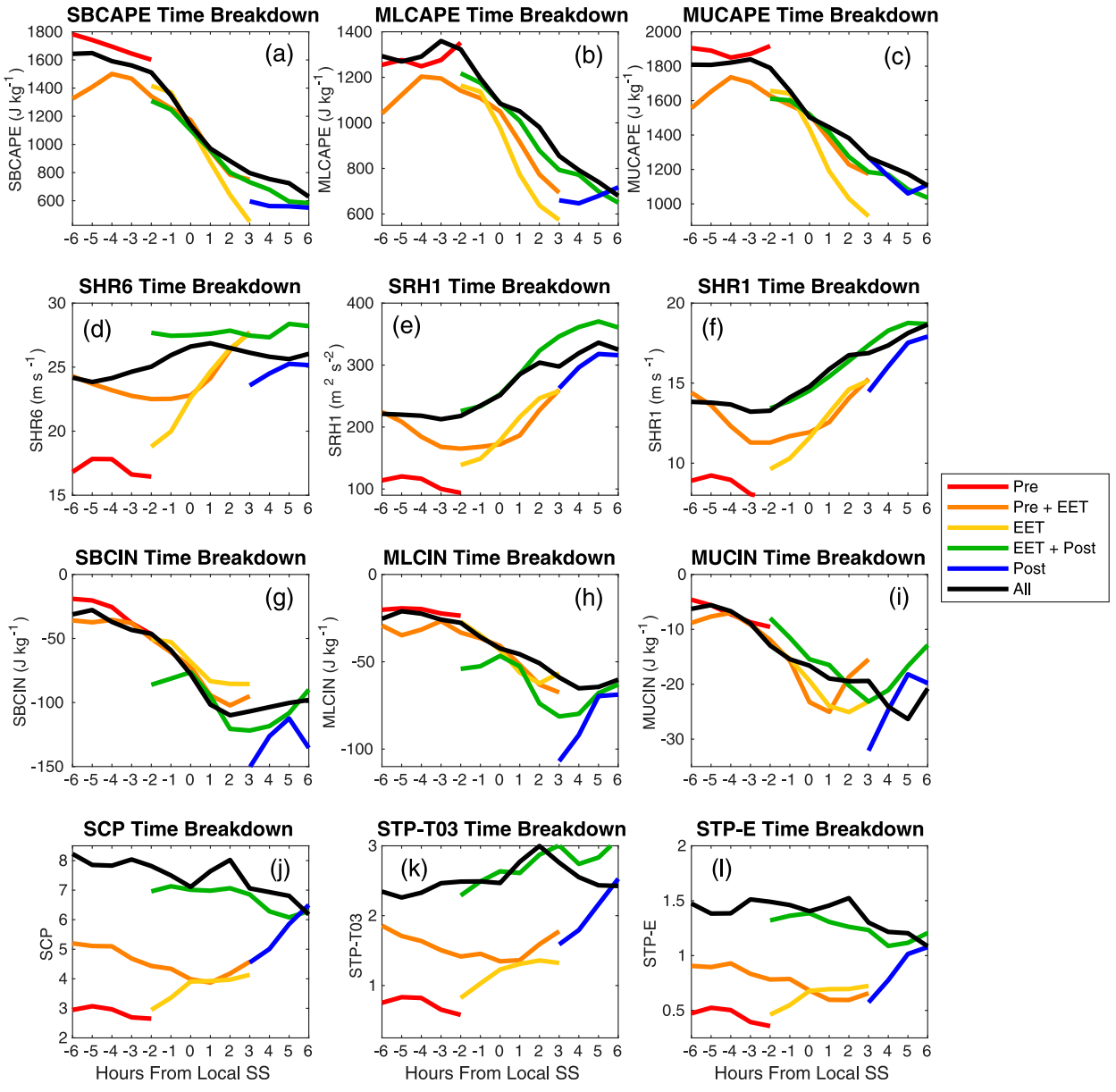

FIG. 9. Time series of average hourly (a)–(c) SB/ML/MUCAPE (J kg^{-1}); (d) 0–6-km SHR (m s^{-1}); (e) 0–1-km SRH (m^2 s^{-2}); (f) 0–1-km SHR (m s^{-1}); (g)–(i) SB/ML/MUCIN (J kg^{-1}); and (j)–(k) SCP, STP-T03, and STP-E (all unitless), respectively, corresponding to each of the analyzed temporal categories. A 2-h moving average is applied to smooth the hourly mean data.

characteristics and low-level SR flow that could influence the thermodynamic and kinematic characteristics of these updrafts.

The raw variables used to characterize the near-storm environments of the analyzed storms are shown in supplemental Table 2 (Peters et al. 2020a).[4] A number of preexisting derived metrics were also considered, including STP-T03, fixed-layer STP as defined in SHARPpy (STP-F; Blumberg et al. 2017), STP-F appended with an SBCIN scaling term (STP-FCIN), STP-E, and effective layer STP with 0–500-m SRH (STP500; Coffer et al. 2019). An alternate version of STP500 is also tested (denoted STP500*), in which the EIL base criteria is loosened such that the metric is only set to zero if the majority of the EIL lies outside the 0–500 m layer (i.e., effective inflow base, or Eff Base > 250 m). Also tested were the Craven–Brooks significant severe parameter (Sig-Sev; Craven et al. 2004), energy helicity index utilizing MLCAPE and SRH3 (EHI; Hart and Korotky 1991), enhanced stretching potential (ESP; Blumberg et al. 2017),

[4] Storm-relative (SR) flow for categories including supercells are computed using Bunkers right mover storm motion vector (Bunkers et al. 2000), whereas QLCS-specific categories use Corfidi downshear vector (Corfidi 2003). SRH, however, is uniformly computed relative to the Bunkers RM vector.

TABLE 2. Storm report count for each mutually exclusive temporal category (e.g., Pre, EET, Post, and combinations thereof) in each of their associated periods.

Day classification	No. of reports (Pre)	No. or reports (EET)	No. of reports (Post)
Pre only	499	—	—
Pre and EET	993	682	—
EET only	—	751	—
EET and post	—	538	409
Post only	—	—	171
All periods	805	1523	616

SCP, CIN-scaled SCP (CSCP; Gropp and Davenport 2018), SHERBE and SHERBS3 (Sherburn and Parker 2014), and theta-E index (TEI) to diagnose potential instability (Blumberg et al. 2017). It is worth noting that the primary purpose of these non-STP parameters is not to distinguish between nontornadic and tornadic environments, so comparisons with STP parameters must be taken with that consideration in mind.

To assess the skill of each variable in distinguishing between tor/sigtor and nontor events, the true skill statistic (TSS; Wilks 2011) is computed over a range of thresholds, following

$$\mathrm{TSS} = \frac{ad - bc}{(a + c)(b + d)}, \tag{1}$$

where a represents the sum of correct tor/sigtor forecasts, b represents the sum of incorrect tor/sigtor forecasts, c represents the sum of correct nontor forecasts, and d represents the sum of incorrect nontor forecasts. A more detailed description of this process is shown in Fig. 11. Given that TSS calculations are prone to "hedging" when used to predict too rare of events (Doswell et al. 1990), categories are only considered if their nonevent to event ratio (i.e., nontor to tor/sigtor) does not

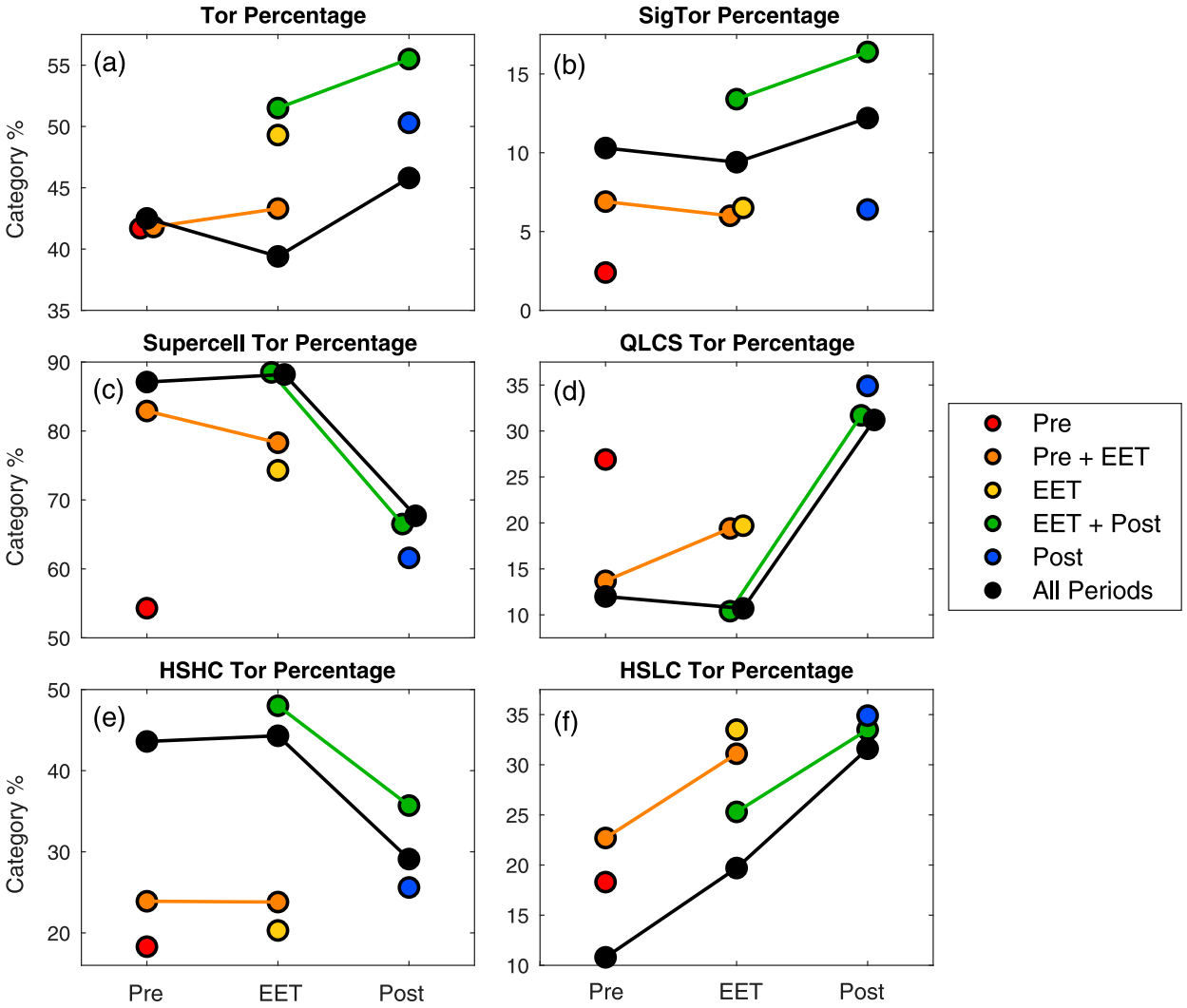

FIG. 10. Breakdown of (a),(b) tornado and significant tornado report percentages, as well as the fraction of those tornadoes that were (c) supercellular, (d) QLCS, (e) HSHC, or (f) HSLC in each of the temporal categories in Fig. 9; the overall report counts associated with each temporal category (and associated periods) can be found in Table 1.

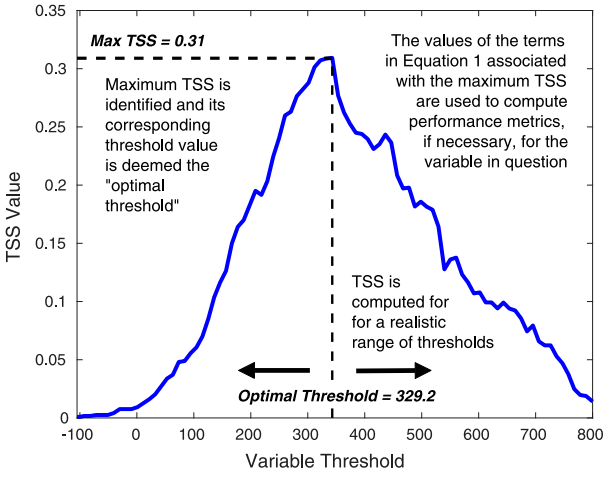

FIG. 11. Sample TSS curve (corresponding to SRH1 for HSLC sigtors, with threshold values in $m^2 s^{-2}$), with explanation of the procedure used to determine the optimal variable threshold and associated metrics. Note, the performance metrics discussed are computed using the terms in Eq. (1) corresponding to the maximum TSS.

exceed 10:1. Heidke skill scores (Wilks 2011) were also computed, and similar predictors were identified, albeit with lower skill scores.

Table 3 contains the highest raw and derived-variable TSS magnitudes associated with HSHC and HSLC tor environments and their predominant modes, and associated variable thresholds. Bolded values indicate a variable whose maximum TSS value was negative, implying that there is maximized skill for values *less* than the provided threshold. In general, HSLC TSS values are uniformly lower than HSHC values, consistent with previous studies (e.g., Anderson-Frey et al. 2019) noting the decreased predictability of HSLC tornadoes (relative to HSHC tornadoes). This lack of predictability is most evident for HSLC QLCS tornadoes. SRH1 shows the most skill of the tested SHR and SRH quantities across almost all categories, while SB/MLLCL shows the most consistent skill among thermodynamic variables. The remaining HSHC predictors mostly comprise other low-level dynamic variables, whereas HSLC categories contain a number of thermodynamic variables including precipitable water (PW) and DCAPE (and perhaps 700–500-hPa lapse rate, LR75, by extension)—consistent with earlier discussion regarding HSLC Post storm environments (supplemental Fig. 3). HSLC supercells are specifically predicted by both SBCAPE and 0–3-km CAPE (3CAPE) as well as Eff Base, while HSLC QLCSs are predicted by Eff/MLCIN. Regarding derived variables, STP-T03 is the best tornadic discriminator across all HSHC categories, as well as for HSLC QLCS, with other STP parameters (viz., STP-E and STP500) and SCP also showing consistent skill. Fixed-layer STP quantities, especially STP-FCIN, are useful HSLC predictors, perhaps due to the HSLC CIN patterns presented earlier (Fig. 4).

Table 4 contains the same information as Table 3, but instead distinguishing between sigtor and nontor environments. Nearly all categories, regardless of environment, show 0–500 m, 0–1 km, 0–3 km, and effective-layer shear and SRH as valuable sigtor predictors. Deep-layer shear (SHR6) and 0–1-km SR flow only show predictive strength for HSHC environments, while SBCAPE, Eff Base, and PW show unique skill across both HSLC categories. In terms of modal patterns, 0–500-m quantities take on greater relative importance for supercells (compared to overall categories) and increased 0–1-km lapse rate (LR1) shows specific skill for HSLC supercells. Similar to the tor results, STP-T03 is generally the most skillful derived metric, with STP-F also providing skill for HSLC supercells. These results highlight that traditional STP metrics still have forecasting value for the Southeast, even in HSLC environments. That being said, their most skillful values are below standard guidance (i.e., STP ~ 1), as previously noted in Sherburn and Parker (2014). For both tor and sigtor (particularly HSLC categories), STP500* outscores the original STP500 formulation, possibly due to the fact that while lower Eff Base is a tornadic predictor, this within itself implies Eff Base values greater than zero. Furthermore, while SHERBE and SHERBS3 have superior skill discriminating between significant severe and nonsevere HSLC environments (their intended purpose), they do not improve on STP metrics in distinguishing between HSLC tor/sigtor and nontor environments.

Comparing Tables 3 and 4, we see a shift from more thermodynamic tor predictors to more kinematic sigtor predictors, with HSHC sigtor predictors comprised entirely of deep-layer and low-level shear and SRH quantities. HSLC sigtor categories still maintain some of the thermodynamic predictors from Table 3, such as PW, SBCAPE, and Eff Base, but low-level shear and SRH quantities have now superseded these variables in predictive skill. Overall, TSS scores for sigtor predictors are higher than those of the tor predictors, as expected given that the tor category includes environments of weak (i.e., F/EF0–1) tornadoes, which have been shown to more strongly resemble nontornadic environments (Thompson et al. 2003). Both the HSHC and HSLC subsets of QLCS sigtors are not shown since they violate the event ratio criteria discussed earlier, but they share the same general predictors as the QLCS results in Table 3 with a skew toward SRH quantities (especially SRH3 and Eff SRH). Despite the overall improvements in sigtor prediction using SRH500 in Coffer et al. (2019), only HSLC supercell shows SRH500 as the highest ranked SRH variable. Moreover, the original formulation of STP500 only shows enhanced skill in HSHC environments, and is outperformed by the alternate formulation in every presented tor/sigtor category. If we consider the thresholds of the presented variables, we see that for both tor and sigtor environments nearly all shear and SRH quantities show noticeably higher thresholds for HSLC categories (relative to HSHC categories), again highlighting the importance of low-level dynamic support for HSLC tornadogenesis. This is particularly intriguing for Eff SRH, given that the low CAPE constraint corresponds to shallower EILs and lower equilibrium level heights, which would act to reduce Eff SRH (all else held constant).

We also considered the TSS results for a given mode and/or environment across each temporal period (supplemental Tables 3–7), in order to see if the variables relevant to

TABLE 3. Environmental (top portion) and derived (bottom portion) tor predictors ranked by maximum TSS magnitude (with associated variable threshold shown in parentheses); bolded values indicate a maximum TSS value whose sign was negative. The variables (and their associated units) are as follows: shear/SR-flow quantities ($m\,s^{-1}$), SRH quantities ($m^2\,s^{-2}$), CAPE/CIN quantities ($J\,kg^{-1}$), lapse rates ($K\,km^{-1}$), LCL/LFC/Eff base quantities (m AGL), PW (in.), RH (%), and derived variables (dimensionless).

HSHC		HSLC		HSHC supercell		HSLC supercell		HSHC QLCS		HSLC QLCS	
Environmental tor predictors											
SRH1	0.44 (244.9)	PW	0.236 (1.4)	SRH1	0.439 (201.1)	PW	0.264 (1.4)	SRH1	0.471 (271)	PW	0.227 (1.4)
SHR1	0.414 (13.5)	DCAPE	**0.171 (372)**	SHR1	0.419 (13.5)	DCAPE	**0.212 (511.1)**	SHR1	0.471 (15.7)	MLLCL	**0.201 (689.8)**
SRH3	0.408 (284.1)	SRH1	0.163 (294.3)	SRH500	0.378 (132.2)	SRH1	0.21 (294.4)	SRH3	0.459 (324.2)	DCAPE	**0.183 (362)**
Eff SRH	0.389 (242.3)	SBCAPE	0.16 (146.1)	SRH3	0.373 (284.3)	LR1	0.21 (3.8)	Eff SRH	0.425 (290.7)	LR75	**0.166 (6.2)**
SRH500	0.38 (137.7)	Eff Base	**0.158 (15.9)**	Eff SRH	0.363 (242.8)	SBCAPE	0.202 (15.8)	MLLCL	**0.419 (660.7)**	Eff CIN	0.144 (−10.6)
SHR500	0.346 (10)	LR75	**0.158 (6.2)**	SHR500	0.362 (9.6)	SRH500	0.197 (164.1)	SRH500	0.393 (137.9)	RH SFC	0.14 (85.4)
MLLCL	**0.3 (757.3)**	Eff SRH	0.158 (285.2)	SBLCL	**0.324 (512.1)**	3CAPE	0.191 (5.6)	SHR3	0.391 (19.9)	MLCIN	0.135 (−65.8)
SHR3	0.298 (19.8)	SRH3	0.156 (371.3)	RH SFC	0.315 (77.8)	Eff Base	**0.187 (170.3)**	SHR500	0.367 (10.2)	SBLCL	**0.133 (434.9)**
SBLCL	**0.284 (512.3)**	MLLCL	**0.152 (669.8)**	MLLCL	**0.299 (785.3)**	SHR1	0.169 (16.4)	RH SFC	0.359 (84.1)	LR85	**0.128 (6)**
SR500	0.281 (16)	MLCIN	0.144 (−62.9)	LR1	**0.282 (7.9)**	SHR500	0.163 (8.7)	SBLCL	**0.32 (456.9)**	SRH3	0.124 (384.5)
Derived tor predictors											
STP-T03	0.419 (3.6)	STP-FCIN	0.233 (0.1)	STP-T03	0.398 (3.6)	STP-FCIN	0.281 (0.1)	STP-T03	0.438 (4.8)	STP-T03	0.176 (0.6)
STP-E	0.336 (2.5)	STP-F	0.214 (0.1)	STP500*	0.327 (2.4)	STP-F	0.275 (0.2)	EHI	0.391 (2.8)	STP-FCIN	0.146 (0.1)
STP500*	0.336 (2.6)	STP-T03	0.205 (0.8)	STP500	0.315 (2.4)	STP500*	0.202 (0.4)	SCP	0.372 (10.8)	STP500*	0.135 (0.2)
STP500	0.331 (2.6)	STP500*	0.189 (0.3)	STP-E	0.286 (1.9)	STP-T03	0.181 (0.8)	STP-E	0.355 (2.4)	STP-F	0.122 (0.1)
SCP	0.33 (11.6)	EHI	0.162 (0.4)	SCP	0.284 (13.2)	EHI	0.18 (0.6)	CSCP	0.353 (10.8)	CSCP	0.106 (1.8)

TABLE 4. As in Table 3, but for sigtor predictors.

HSHC		HSLC		HSHC supercell		HSLC supercell	
Environmental sigtor predictors							
SRH1	0.576 (247.2)	SRH1	0.31 (329.2)	SRH1	0.562 (243.3)	SRH500	0.358 (198.4)
SRH3	0.546 (324.1)	Eff SHR	0.306 (23.4)	SHR1	0.538 (14.7)	SRH1	0.348 (329.2)
SHR1	0.537 (14.7)	SRH500	0.292 (211.6)	SRH500	0.521 (171)	SHR1	0.348 (19.6)
Eff SRH	0.534 (286.1)	SHR1	0.284 (19.6)	SHR500	0.513 (10.5)	SHR500	0.295 (13.4)
SRH500	0.528 (174.7)	SRH3	0.277 (415.3)	SRH3	0.502 (324.3)	Eff SRH	0.279 (365.5)
SHR500	0.48 (10.5)	Eff SRH	0.273 (315.5)	Eff SRH	0.499 (286.3)	SRH3	0.276 (372.3)
SR500	0.456 (16.2)	SBCAPE	0.24 (154.4)	SR500	0.406 (16.2)	Eff Base	**0.267 (276.8)**
SHR3	0.443 (21)	SHR500	0.232 (13.4)	SHR3	0.388 (23.2)	SBCAPE	0.264 (80.7)
SHR6	0.392 (26.9)	Eff Base	**0.229 (41.7)**	SHR6	0.344 (29.2)	LR1	0.253 (3.9)
SR1	0.39 (14)	PW	0.222 (1.4)	SR1	0.34 (14)	PW	0.252 (1.4)
Derived sigtor predictors							
STP-T03	0.597 (4.4)	STP-T03	0.357 (0.9)	STP-T03	0.57 (4.2)	STP-F	0.399 (0.2)
STP500*	0.507 (2.7)	STP500*	0.344 (0.4)	STP500*	0.476 (2.7)	STP500*	0.394 (0.4)
STP-E	0.504 (2.3)	STP-F	0.337 (0.3)	STP500	0.458 (2.6)	STP-FCIN	0.376 (0.1)
SCP	0.5 (13.2)	STP-FCIN	0.337 (0.1)	SCP	0.451 (13.2)	STP-T03	0.35 (0.8)
STP500	0.495 (2.6)	EHI	0.286 (0.4)	CSCP	0.443 (13.2)	EHI	0.321 (0.7)

tornadogenesis change as a function of time (e.g., thermodynamic variables become more relevant as environmental CAPE decreases). However, the interpretation of these results is made difficult by the diurnal CAPE and shear trends shown earlier (Figs. 2–9) and associated changes in environment and mode (Figs. 10c–f). For instance, if we consider the evolution of predictors, they resemble supercell/HSHC predictors in the pre-transition, but look increasingly like HSLC/QLCS predictors by the post-transition. Classifying further by time, environment, and mode, though scientifically interesting, limits sample size such that TSS results become dubious. Therefore, it is best to only consider the environment-mode combinations presented, with the foreknowledge that they inherently carry some temporal information.

The final question that remains is whether the prediction of SE tornadoes can be advanced by way of these TSS results. To this end, we construct a number of new STP parameters for each of the four categories shown in Table 4, as well as QLCS tornado parameters (since no QLCS sigtor categories met our event ratio criteria). As we are not partitioning our data into separate training and verification subsets, fivefold cross validation[5] is performed to ensure that the initial TSS results are not simply a by-product of this particular dataset, and can instead generalize to other tested datasets (in this case, subsamples of the original data). This process is accomplished by randomly sampling 80% of the reports for a given category, computing associated TSS and threshold values, and constructing the parameter using the most skillful variables. Correlation analysis is performed on the variables considered for each parameter to ensure they are independent, with the exception of low-level SRH and deep-layer shear. Note that CAPE variables largely do not appear in these new parameters as a result of already partitioning between low and high CAPE. If the top ranked variables change between folds (i.e., a different SRH quantity ranks highest), they are also tested, and the more skillful variable is retained. These variables are then normalized using optimal thresholds motivated by the TSS analysis, such that parameter values ≥ 1 represent increased likelihood of their associated hazard. This parameter is then tested on the remaining 20% of the reports for each fold to determine its performance metrics. Both the training and testing report subsets associated with each fold are required to meet the established event ratio criteria.

Following the design of previous STP metrics, such as STP-T03 and STP-E, all deep-layer shear terms (e.g., SHR6, Eff SHR) in the resultant parameters are capped at a value of 1.5.[6] Also following the treatment of LCL and CIN terms in previous STP metrics, all thermodynamic terms are capped at a value of 1 and negative values are set to 0 (unless otherwise stated). The HSHC parameter is as follows:

$$\mathrm{STP(HSHC)} = \frac{\mathrm{SRH1}}{250\,\mathrm{m^2\,s^{-2}}} \times \frac{\mathrm{SHR6}}{27.5\,\mathrm{m\,s^{-1}}} \times \frac{1500 - \mathrm{SBLCL}}{1000\,\mathrm{m}} \times \frac{1500 - \mathrm{DCAPE}}{750\,\mathrm{J\,kg^{-1}}}. \quad (2)$$

The HSHC supercell (SC) version of this STP is similar, except the DCAPE term is removed and the SRH1 and SHR6 thresholds are adjusted to $225\,\mathrm{m^2\,s^{-2}}$ and $30\,\mathrm{m\,s^{-1}}$, respectively. The HSLC STP parameter substitutes Eff SHR for SHR6 and adds SBCAPE and PW terms, as follows[7]:

[5] The 10-fold cross validation was also tested. The resulting variable rankings were virtually identical to those identified with fivefolds, but the limited size of the testing dataset led to large variability in the performance of the metrics constructed with these rankings.

[6] Note that there is no explicit lower bound for this shear term, since our CAPE/shear classification implicitly sets a lower bound.

[7] The SBCAPE term is capped at 2.

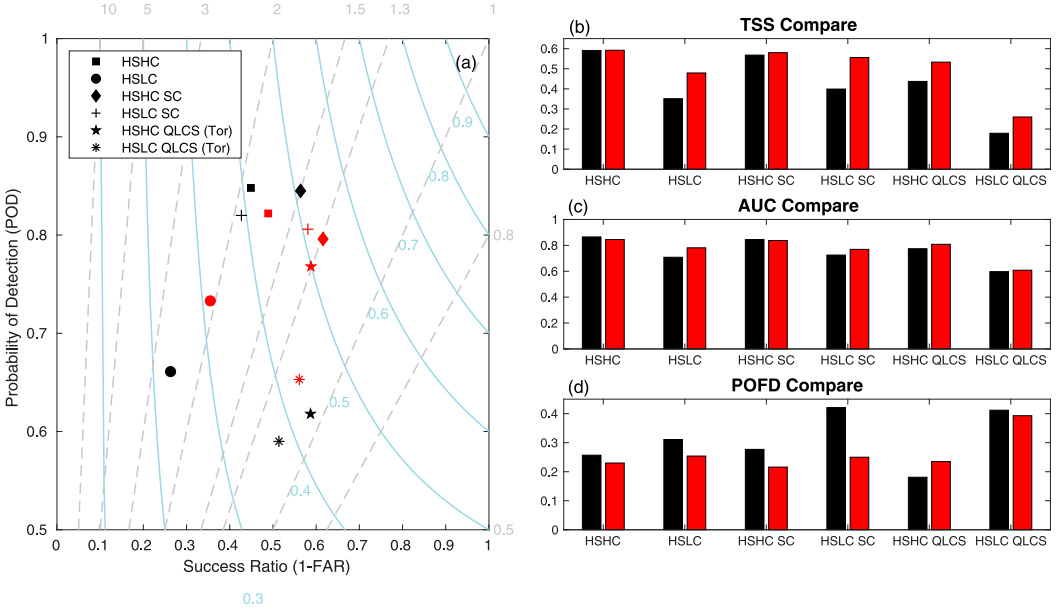

FIG. 12. (a) Performance diagram for the most skillful preexisting metrics for each analyzed category from Tables 2–3 (in black) and the new STP and QLCS Tor metrics (in red). The displayed values of probability of detection (POD) and success ratio are those associated with the maximum TSS values for each metric. Forecast bias is shown in dashed gray lines, and critical success index (CSI) is shown in light blue lines. Note that the *y* axis begins at a POD of 0.5 to highlight differences between metrics; also shown are comparisons of (b) true skill statistic (TSS), (c) area under curve (AUC), and (d) probability of false detection (POFD) for the presented metrics.

$$\text{STP(HSLC)} = \frac{\text{SRH1}}{325\,\text{m}^2\,\text{s}^{-2}} \times \frac{\text{Eff SHR}}{25\,\text{m s}^{-1}} \times \frac{\text{SBCAPE}}{150\,\text{J kg}^{-1}} \times \frac{\text{PW}}{1.4\,\text{g kg}^{-1}}. \tag{3}$$

The HSLC SC STP substitutes SRH500 for SRH1 and replaces SBCAPE with Eff Base, simplifying as follows[8]:

$$\text{STP(HSLC SC)} = \frac{\text{SRH500}}{200\,\text{m}^2\,\text{s}^{-2}} \times \frac{500 - \text{Eff Base}}{250\,\text{m}} \times \frac{\text{PW}}{1.4\,\text{g kg}^{-1}}. \tag{4}$$

The construction of the HSHC and HSLC QLCS tor parameters (HSHC-Q and HSLC-Q, respectively) was less straightforward, given the inherently decreased predictability of these phenomena, with few variables providing consistently high skill. For HSHC-Q, a simple combination of SRH1 and and MLLCL proved most skillful, as follows:

$$\text{HSHC}-\text{Q} = \frac{\text{SRH1}}{275\,\text{m}^2\,\text{s}^{-2}} \times \frac{2000 - \text{MLLCL}}{1400\,\text{m}}. \tag{5}$$

HSLC-Q retains the LCL term (with adjusted thresholds), but adds PW and DCAPE,[9] as follows:

$$\text{HSLC}-\text{Q} = \frac{1600 - \text{MLLCL}}{1000\,\text{m}} \times \frac{1200 - \text{DCAPE}}{800\,\text{J kg}^{-1}} \times \frac{\text{PW}}{1.4\,\text{g kg}^{-1}}. \tag{6}$$

Figure 12 shows the performance diagram (Roebber 2009) containing the POD and success ratio (1 − FAR) corresponding to these new metrics, as well as the top preexisting metrics for each of the analyzed categories (as shown in Tables 3–4). Comparisons between the TSS values, area under curve (AUC) values associated with the receiver operating characteristic (ROC; Mason 1982) curves, and probability of false detection (POFD) for these metrics are also included. The new HSHC STP metrics show minimal improvement over STP-T03, which is not entirely surprising given that most existing STP metrics have been formulated with this sort of environment (e.g., ample instability and shear) in mind. HSLC STP shows marked improvement, with both increases in POD, success ratio and TSS, and decreases in POFD. Both QLCS parameters show increases in POD (and by extension, TSS), though no appreciable change in success ratio.

4. Discussion and conclusions

a. Summary of results

Now that we have examined the evolution of SE nocturnal storm environments and the predictability of their tornadoes, we will revisit the questions we set out to address within the context of the literature. The first of these was simply: how do

[8] The Eff Base term is set to zero for Eff Base > 250 m, as in our formulation of STP500*.

[9] All thermodynamic terms in both HSHC-Q and HSLC-Q are capped at a value of 1.

storm environments evolve across the EET? When severe convection persists across the EET, its associated environment typically displays a gradual decrease in CAPE (Fig. 2a–i) and an increase in static stability (Fig. 4), accompanied by increases in low-level shear and SRH (Fig. 3). However, the shape and magnitude of these trends can vary as a function of the average CAPE/shear characteristics in the near-storm environment. When the pre-transition or EET environments exhibit HSLC conditions, associated storm environments tend to exhibit larger deep-layer shear and low-level shear/SRH values for the remainder of the day relative to HSHC environments. Furthermore, many of these HSLC environments actually destabilize as the evening progresses, which along with associated CAPE increases resemble the evolution detailed in King et al. (2017). These CAPE increases and CIN magnitude decreases are strongly correlated with increases in low-level θ_e and LR1 (supplemental Fig. 1), respectively, which underscore the importance of low-level warm air and/or differential advection (as in King et al. 2017) and steepened low-level lapse rates (as in Sherburn and Parker 2014) for HSLC storm maintenance. The sum total of these factors likely plays a compensatory role given reduced instability, allowing HSLC convection to persist and produce hazards well into the evening. However, some of these compensating factors were primarily attributed to QLCS modes (Figs. 6–8), such that the factors contributing to HSLC supercell maintenance are less clear.

We also explored how environmental variables evolve when severe convection fails to persist into and past the EET to determine what factors potentially govern nocturnal storm maintenance. Days in which severe convection persisted into and through the EET show initially larger shear and SRH values (Figs. 9d–f), as well as slower decreases in CAPE (Figs. 9a–c) and slower increases in CIN magnitude (Figs. 9g–i, particularly ML/MUCIN) across the EET. These results share some similarities with the findings of Gropp and Davenport (2018) (cf. their Fig. 9), suggesting that these observations regarding nocturnal storm maintenance may hold true in a broader sense for different storm modes and geographical regions.

Our next question asked whether the presented environmental evolution can influence the prevalence and convective mode of tornadoes. HSLC pre-transition conditions were found to initially suppress tornadoes, but increase the prevalence of tornadoes later in the day (Fig. 5a), possibly in response to associated SRH and CIN patterns. With respect to mode, HSHC conditions generally favor supercellular tornadoes, while HSLC conditions in a given period increasingly favor the prevalence of QLCS tornadoes later that day (Figs. 5d–f). Similar results hold true even when severe convection fails to persist through the EET, with an uptick in HSLC and QLCS tornadoes into the evening hours (Figs. 10c–f). These findings highlight that CAPE/shear characteristics in a given period can influence the tornado characteristics not only then, but also during subsequent periods.

We then examined which near-storm environment variables most effectively discriminate between tor/sigtor and nontor storm environments. Regardless of environment or mode, low-level shear/SRH quantities (and by extension, SR flow) are consistently skillful predictors for tor/sigtor (Tables 3–4, respectively), as expected. HSLC tornadoes are specifically predicted by moisture-related variables, including increased PW and decreased DCAPE. The former indicates an increase in local moisture, which has been shown in studies such as Mead and Thompson (2011) to preclude the formation of near-surface stable layers via advection of higher θ_e air by the LLJ (as in Maddox 1983). This slowed CIN development—perhaps related to the presented destabilization of HSLC environments (Figs. 4a,b)—would facilitate storm maintenance into evening hours (Gropp and Davenport 2018), thus increasing the likelihood of nocturnal tornadogenesis (Mead and Thompson 2011).

Interpretation of the latter, DCAPE, is less straightforward. Decreased DCAPE may be related to reduced evaporation (perhaps aided by the local moisture enhancements discussed earlier) and less negatively buoyant outflow, though we must be careful drawing direct comparison between the two due to entrainment effects (Gilmore and Wicker 1998). Such a relationship would be physically plausible, given the favorable influence of less negatively buoyant outflow on supercell tornadogenesis (e.g., Markowski et al. 2002; Shabbott and Markowski 2006), primarily by making it easier for near-surface parcels to be dynamically lifted. Furthermore, this prevents outflow from undercutting low-level circulations and reducing the ability of their associated dynamic pressure accelerations to stretch and converge near-surface rotation (Markowski and Richardson 2014; Brown and Nowotarski 2019). Even for nonsupercellular tornadoes, less negatively buoyant outflow may allow QLCS updrafts to remain upright rather than sloping back over their attendant cold pools (Rotunno et al. 1988), a crucial ingredient for QLCS tornadogenesis (e.g., Schaumann and Przybylinski 2012; Williams et al. 2018). That being said, the exact relationship between observed HSLC cold pool deficits and tornadogenesis remains unclear (McDonald and Weiss 2021). In addition to the aforementioned variables, HSLC tornadic supercells also exhibit increased LR1 consistent with previous HSLC studies (e.g., Sherburn and Parker 2014; Sherburn et al. 2016), along with lowered Eff Base and increased SBCAPE and 3CAPE. These findings imply that with reduced environmental instability, SE tornadogenesis becomes particularly sensitive to low-level thermodynamic characteristics and the ability for storms to remain more surface based.

In terms of existing forecasting metrics, STP-T03 shows the highest skill for both tor and sigtor across nearly every environment-mode combination. This is somewhat surprising, given that more recent iterations of STP incorporating effective-layer quantities and SRH500 are generally thought to be improvements upon this original STP formulation. That said, Table 4 in Coffer et al. (2019) indicated that the second lowest skill for STP500 was across the lower MS Valley (LVM), so this insight is consistent with past work. For HSLC supercells, STP-F and STP-FCIN are effective predictors, due perhaps to their inclusion of more surface-based quantities (SBLCL and SBCAPE). Finally, a number of new STP and QLCS tor metrics were also developed. Admittedly, there is minimal room for such improvement with HSHC categories, since most STP parameters are designed for prototypical

convective environments with appreciable shear and instability. Noticeable improvements can be made, however, for HSLC/HSLC SC sigtor categories with the addition of predictors such as PW and Eff Base. Note that these parameters have only been constructed and evaluated numerically. More in depth analysis, including a 2D spatial assessment of these new parameters relative to traditional STP parameters and observed storm reports, is necessary before such parameters can reliably be put into practice. In particular, one needs to consider that these new parameters are conditioned on the occurrence of storms within specific CAPE regimes, and therefore could incur large false alarm rates if applied blindly.

b. *Considerations and limitations*

As with any study using near-storm model soundings as a proxy for observations, there are a number of limitations that must be considered. First is the potential for error in the sounding-derived data ascribed to each severe convective report. These errors could stem from the underlying model output, such as the near-surface cool and dry biases of the RUC model, which can lead to underestimates of CAPE on the order of 100–250 J kg^{-1} (e.g., Thompson et al. 2003, their Fig. 3). Similar magnitude variability in CAPE calculations can also result from the method used to lift parcels and compute their θ_e upon saturation. For instance, Coffer et al. (2019) noted that CAPE values computed with NSHARP/SHARPpy—like those used in this study—tend to be higher than most other computational methods, particularly for high CAPE soundings. Both sources could introduce uncertainty into the CAPE/shear classification of individual reports, as well as our characterization of CAPE and CIN evolution. Overestimates of CAPE would lend confidence to our characterization of low-CAPE environments but bring into question our high-CAPE classification (and vice versa with underestimates). Though worth consideration, the design of our two environmental categories helps limit this uncertainty. For instance, if we perturb our calculated CAPE values by the maximum error bound in the above literature (250 J kg^{-1}), less than 1% of the cases in either category switch classification (e.g., HSHC switching to HSLC, or vice versa).

There are also potential spatiotemporal errors associated with the mesoanalyses utilized. The 40-km spacing and hourly time step could ascribe inaccurate data to reports occurring near tight gradients (e.g., baroclinic zones), and also smooth out relevant small-scale features like the narrow bands of moist instability shown in King et al. (2017) to be important for sustaining HSLC convection. For studies like this compositing environments across large report samples, the net impact of the discussed biases may ultimately be small (e.g., Thompson et al. 2003; Thompson et al. 2012), but it is important to understand that the statistic robustness afforded by larger datasets does not always translate to practical relevance for forecasting, as noted in Anderson-Frey et al. (2016).

From a methodology standpoint, there is a great deal of subjectivity when applying fixed CAPE/shear environmental thresholds. Though physically motivated, the HSHC/HSLC definitions developed herein (and in the literature) are somewhat arbitrary constructs used to isolate and analyze unique subsets of the storm climatology. Both represent only portions of a much broader CAPE/shear parameter space in which Southeast severe convection and tornadoes can exist (e.g., Anderson-Frey et al. 2019, their Fig. 2a), as demonstrated by the uniformly favorable impact of high-shear, moderate-CAPE conditions for tor/sigtor prevalence noted in section 3b. Furthermore, the CAPE values which qualify as "high" or "low" vary by (and even within) geographical regions (Thompson et al. 2013). Also worth consideration is our EF2+ cutoff for significant tornadoes. Though largely consistent with previous observational tornado studies, its utility for the SE tornado climatology is debatable. Thompson et al. (2017), particularly their Fig. 14, demonstrated that low-level rotational velocities are approximately 10 kt lower in MS/AL for the same EF-scale ratings compared to the Great Plains, perhaps due to the relative lack of potential damage indicators in much of the Great Plains, with some accompanying potential for tornadoes to be underrated by the EF scale (away from urban areas). As such, a stricter significant tornado criterion of EF3+ might be warranted for the SE to help avoid the conflation of some weak and significant tornadoes. For instance, roughly 93% of the QLCS sigtors identified by our original criteria have an EF2 rating. This helps to explain their inherent lack of predictability, but it also suggests that QLCS tornadoes may be a less impactful portion of the overall SE tornado climatology than commonly thought, particularly given the aforementioned potential for biases in damage ratings in this region.

c. *Future work*

There are numerous avenues for future research that would build upon and contextualize the results presented in this study. For instance, it might prove useful to repeat similar analyses for other geographical regions in order to gauge the uniqueness of our SE results, and help advance a unified theory regarding the storm maintenance and tornadogenesis potential of storms persisting across the EET. Breaking the presented analyses down by season may also reveal additional findings, given the seasonal variability of SE storm environments shown in Anderson-Frey et al. (2019). Furthermore, numerical simulations could help determine the net impact of the increased low-level SRH and nocturnal destabilization on low-level updraft forcing in HSLC storm environments in spite of overall limited buoyancy. Paired with the base-state substitution (BSS) technique of Davenport et al. (2019), such simulations could provide storm-scale insight into how environmental evolution across the EET influences the dynamical processes relevant for HSLC tornadogenesis.

Acknowledgments. The authors thank Ryan Jewell for his assistance in retrieving the raw sounding data associated with the analyzed storm reports, as well as the three anonymous reviewers whose input benefited the clarity and quality of this manuscript. M. Brown and C. Nowotarski's efforts were supported by the National Science Foundation (NSF) Grant AGS-1928319 and J. Peters was supported by AGS-1928666.

Data availability statement. The storm report data utilized in this study came from the SPC convective mode-environment

dataset developed in Thompson et al. (2012). All analysis code is archived locally and available upon request to the corresponding author.

REFERENCES

Anderson-Frey, A. K., Y. P. Richardson, A. R. Dean, R. L. Thompson, and B. T. Smith, 2016: Investigation of near-storm environments for tornado events and warnings. *Wea. Forecasting*, **31**, 1771–1790, https://doi.org/10.1175/WAF-D-16-0046.1.

——, ——, ——, ——, and ——, 2019: Characteristics of tornado events and warnings in the southeastern United States. *Wea. Forecasting*, **34**, 1017–1034, https://doi.org/10.1175/WAF-D-18-0211.1.

Ashley, W. S., A. J. Krmenec, and R. Schwantes, 2008: Vulnerability due to nocturnal tornadoes. *Wea. Forecasting*, **23**, 795–807, https://doi.org/10.1175/2008WAF2222132.1.

——, A. M. Haberlie, and J. Strohm, 2019: A climatology of quasi-linear convective systems and their hazards in the United States. *Wea. Forecasting*, **34**, 1605–1631, https://doi.org/10.1175/WAF-D-19-0014.1.

Benjamin, S. G., and Coauthors, 2004: An hourly assimilation–forecast cycle: The RUC. *Mon. Wea. Rev.*, **132**, 495–518, https://doi.org/10.1175/1520-0493(2004)132<0495:AHACTR>2.0.CO;2.

——, and Coauthors, 2016: A North American hourly assimilation and model forecast cycle: The Rapid Refresh. *Mon. Wea. Rev.*, **144**, 1669–1694, https://doi.org/10.1175/MWR-D-15-0242.1.

Billings, J. M., and M. D. Parker, 2012: Evolution and maintenance of the 22–23 June 2003 nocturnal convection during BAMEX. *Wea. Forecasting*, **27**, 279–300, https://doi.org/10.1175/WAF-D-11-00056.1.

Blackadar, A. K., 1957: Boundary layer wind maxima and their significance for the growth of nocturnal inversions. *Bull. Amer. Meteor. Soc.*, **38**, 283–290, https://doi.org/10.1175/1520-0477-38.5.283.

Blumberg, W. G., K. T. Halbert, T. A. Supinie, P. T. Marsh, R. L. Thompson, and J. A. Hart, 2017: SHARPpy: An open-source sounding analysis toolkit for the atmospheric sciences. *Bull. Amer. Meteor. Soc.*, **98**, 1625–1636, https://doi.org/10.1175/BAMS-D-15-00309.1.

Bothwell, P. D., J. A. Hart, and R. L. Thompson, 2002: An integrated three-dimensional objective analysis scheme in use at the Storm Prediction Center. Preprints, *21st Conf. on Severe Local Storms*, San Antonio, TX, Amer. Meteor. Soc., J117–J120.

Brown, M. C., and C. J. Nowotarski, 2019: The influence of lifting condensation level on low-level outflow and rotation in simulated supercell thunderstorms. *J. Atmos. Sci.*, **76**, 1349–1372, https://doi.org/10.1175/JAS-D-18-0216.1.

——, and ——, 2020: Southeastern U.S. tornado outbreak likelihood using daily climate indices. *J. Climate*, **33**, 3229–3252, https://doi.org/10.1175/JCLI-D-19-0684.1.

Bunker, R. C., A. E. Cohen, J. A. Hart, A. E. Gerard, K. E. Klockow-McClain, and D. P. Nowicki, 2019: Examination of the predictability of nocturnal tornado events in the southeastern United States. *Wea. Forecasting*, **34**, 467–479, https://doi.org/10.1175/WAF-D-18-0162.1.

Bunkers, M. J., B. A. Klimowski, J. W. Zeitler, R. L. Thompson, and M. L. Weisman, 2000: Predicting supercell motion using a new hodograph technique. *Wea. Forecasting*, **15**, 61–79, https://doi.org/10.1175/1520-0434(2000)015<0061:PSMUAN>2.0.CO;2.

Coffer, B. E., and M. D. Parker, 2015: Impacts of increasing low-level shear on supercells during the early evening transition. *Mon. Wea. Rev.*, **143**, 1945–1969, https://doi.org/10.1175/MWR-D-14-00328.1.

——, ——, R. L. Thompson, B. T. Smith, and R. E. Jewell, 2019: Using near-ground storm relative helicity in supercell tornado forecasting. *Wea. Forecasting*, **34**, 1417–1435, https://doi.org/10.1175/WAF-D-19-0115.1.

Corfidi, S. F., 2003: Cold pools and MCS propagation: Forecasting the motion of downwind-developing MCSs. *Wea. Forecasting*, **18**, 997–1017, https://doi.org/10.1175/1520-0434(2003)018<0997:CPAMPF>2.0.CO;2.

Craven, J. P., and Coauthors, 2004: Baseline climatology of sounding derived parameters associated with deep, moist convection. *Natl. Wea. Dig.*, **28**, 13–24.

Davenport, C. E., and M. D. Parker, 2015: Impact of environmental heterogeneity on the dynamics of a dissipating supercell thunderstorm. *Mon. Wea. Rev.*, **143**, 4244–4277, https://doi.org/10.1175/MWR-D-15-0072.1.

——, C. L. Ziegler, and M. I. Biggerstaff, 2019: Creating a more realistic idealized supercell thunderstorm evolution via incorporation of base-state environmental variability. *Mon. Wea. Rev.*, **147**, 4177–4198, https://doi.org/10.1175/MWR-D-18-0447.1.

Davies, J. M., and A. Fischer, 2009: Environmental characteristics associated with nighttime tornadoes. *Electron. J. Oper. Meteor.*, **10**, 1–29.

Dean, A. R., and R. S. Schneider, 2008: Forecast challenges at the NWS Storm Prediction Center relating to the frequency of favorable severe storm environments. *24th Conf. on Severe Local Storms*, Savannah, GA, Amer. Meteor. Soc., 9A.2, https://ams.confex.com/ams/24SLS/techprogram/paper_141743.htm.

——, and ——, 2012: An examination of tornado environments, events, and impacts from 2003–2012. *26th Conf. on Severe Local Storms*, Nashville, TN, Amer. Meteor. Soc., P60, https://ams.confex.com/ams/26SLS/webprogram/Paper211580.html.

Doswell, C. A., III, R. Davies-Jones, and D. L. Keller, 1990: On summary measures of skill in rare event forecasting based on contingency tables. *Wea. Forecasting*, **5**, 576–585, https://doi.org/10.1175/1520-0434(1990)005<0576:OSMOSI>2.0.CO;2.

Geerts, B., and Coauthors, 2017: The 2015 Plains Elevated Convection At Night Field Project. *Bull. Amer. Meteor. Soc.*, **98**, 767–786, https://doi.org/10.1175/BAMS-D-15-00257.1.

Gilmore, M. S., and L. J. Wicker, 1998: The influence of mid-tropospheric dryness on supercell morphology and evolution. *Mon. Wea. Rev.*, **126**, 943–958, https://doi.org/10.1175/1520-0493(1998)126<0943:TIOMDO>2.0.CO;2.

Gray, K., and J. Frame, 2019: Investigating the transition from elevated multicellular convection to surface-based supercells during the tornado outbreak of 24 August 2016 using a WRF Model simulation. *Wea. Forecasting*, **34**, 1051–1079, https://doi.org/10.1175/WAF-D-18-0209.1.

Gropp, M. E., and C. E. Davenport, 2018: The impact of the nocturnal transition on the lifetime and evolution of supercell thunderstorms in the Great Plains. *Wea. Forecasting*, **33**, 1045–1061, https://doi.org/10.1175/WAF-D-17-0150.1.

Guyer, J. L., and A. R. Dean, 2010: Tornadoes within weak CAPE environments across the continental United States. *25th Conf. on Severe Local Storms*, Denver, CO, Amer. Meteor. Soc., 1.5, https://ams.confex.com/ams/pdfpapers/175725.pdf.

Hart, J. A., and W. Korotky, 1991: The SHARP workstation v1.50 users guide. NOAA/NWS, U.S. Department of Commerce, 30 pp.

Holton, J. R., 1967: The diurnal boundary layer wind oscillation above sloping terrain. *Tellus*, **19**, 200–205, https://doi.org/10.3402/tellusa.v19i2.9766.

Kelly, D. L., J. T. Schaefer, R. P. McNulty, C. A. Doswell III, and R. F. Abbey Jr., 1978: An augmented tornado climatology. *Mon. Wea. Rev.*, **106**, 1172–1183, https://doi.org/10.1175/1520-0493(1978)106<1172:AATC>2.0.CO;2.

King, J. R., M. D. Parker, K. D. Sherburn, and G. M. Lackmann, 2017: Rapid evolution of cool season, low-CAPE severe thunderstorm environments. *Wea. Forecasting*, **32**, 763–779, https://doi.org/10.1175/WAF-D-16-0141.1.

Kis, A. K., and J. M. Straka, 2010: Nocturnal tornado climatology. *Wea. Forecasting*, **25**, 545–561, https://doi.org/10.1175/2009WAF2222294.1.

MacIntosh, C. W., and M. D. Parker, 2017: The 6 May 2010 elevated supercell during VORTEX2. *Mon. Wea. Rev.*, **145**, 2635–2657, https://doi.org/10.1175/MWR-D-16-0329.1.

Maddox, R. A., 1983: Large-scale meteorological conditions associated with midlatitude, mesoscale convective complexes. *Mon. Wea. Rev.*, **111**, 1475–1493, https://doi.org/10.1175/1520-0493(1983)111<1475:LSMCAW>2.0.CO;2.

——, 1993: Diurnal low-level wind oscillation and storm-relative helicity. *The Tornado: Its Structure, Dynamics, and Hazards*, *Geophys. Monogr.*, Vol. 79, Amer. Geophys. Union, 591–598, https://doi.org/10.1029/GM079p0591.

Markowski, P. M., and Y. P. Richardson, 2014: The influence of environmental low-level shear and cold pools on tornadogenesis: Insights from idealized simulations. *J. Atmos. Sci.*, **71**, 243–275, https://doi.org/10.1175/JAS-D-13-0159.1.

——, J. M. Straka, E. N. Rasmussen, and D. O. Blanchard, 1998: Variability of storm-relative helicity during VORTEX. *Mon. Wea. Rev.*, **126**, 2959–2971, https://doi.org/10.1175/1520-0493(1998)126<2959:VOSRHD>2.0.CO;2.

——, ——, and ——, 2002: Direct surface thermodynamic observations within the rear-flank downdrafts of nontornadic and tornadic supercells. *Mon. Wea. Rev.*, **130**, 1692–1721, https://doi.org/10.1175/1520-0493(2002)130<1692:DSTOWT>2.0.CO;2.

——, and Coauthors, 2012: The pretornadic phase of the Goshen County, Wyoming, supercell of 5 June 2009 intercepted by VORTEX2. Part II: Intensification of low-level rotation. *Mon. Wea. Rev.*, **140**, 2916–2938, https://doi.org/10.1175/MWR-D-11-00337.1.

Mason, I., 1982: A model for assessment of weather forecasts. *Aust. Meteor. Mag.*, **30**, 291–303.

McDonald, J. M., and C. C. Weiss, 2021: Cold pool characteristics of tornadic quasi-linear convective systems and other convective modes observed during VORTEX-SE. *Mon. Wea. Rev.*, **149**, 821–840, https://doi.org/10.1175/MWR-D-20-0226.1.

Mead, C., and R. Thompson, 2011: Environmental characteristics associated with nocturnal significant-tornado events in the Great Plains. *Electron. J. Severe Storms Meteor.*, **6** (6), https://www.ejssm.org/ojs/index.php/ejssm/article/viewArticle/84.

Muñoz, E., and D. Enfield, 2011: The boreal spring variability of the Intra-Americas low-level jet and its relation with precipitation and tornadoes in the eastern United States. *Climate Dyn.*, **36**, 247–259, https://doi.org/10.1007/s00382-009-0688-3.

Nowotarski, C. J., P. M. Markowski, and Y. P. Richardson, 2011: The characteristics of numerically simulated supercell storms situated over statically stable boundary layers. *Mon. Wea. Rev.*, **139**, 3139–3162, https://doi.org/10.1175/MWR-D-10-05087.1.

Parker, M. D., 2014: Composite VORTEX2 supercell environments from near-storm soundings. *Mon. Wea. Rev.*, **142**, 508–529, https://doi.org/10.1175/MWR-D-13-00167.1.

Peters, J. M., K. C. Eure, and R. S. Schumacher, 2017: Factors that drive MCS growth from supercells. *17th Conf. on Mesoscale Processes*, San Diego, CA, Amer. Meteor. Soc., 9.6, https://ams.confex.com/ams/17MESO/webprogram/Paper320248.html.

——, C. J. Nowotarski, and H. Morrison, 2019: The role of vertical wind shear in modulating maximum supercell updraft velocities. *J. Atmos. Sci.*, **76**, 3169–3189, https://doi.org/10.1175/JAS-D-19-0096.1.

——, H. Morrison, C. J. Nowotarski, J. P. Mulholland, and R. L. Thompson, 2020a: A formula for the maximum vertical velocity in supercell updrafts. *J. Atmos. Sci.*, **77**, 3747–3757, https://doi.org/10.1175/JAS-D-20-0103.1.

——, C. J. Nowotarski, J. P. Mulholland, and R. L. Thompson, 2020b: The influences of effective inflow layer streamwise vorticity and storm-relative flow on supercell updraft properties. *J. Atmos. Sci.*, **77**, 3033–3057, https://doi.org/10.1175/JAS-D-19-0355.1.

Rasmusson, E. M., 1967: Atmospheric water vapor transport and the water balance of North America. Part I: Characteristics of the water vapor flux field. *Mon. Wea. Rev.*, **95**, 403–426, https://doi.org/10.1175/1520-0493(1967)095<0403:AWVTAT>2.3.CO;2.

Roebber, P. J., 2009: Visualizing multiple measures of forecast quality. *Wea. Forecasting*, **24**, 601–608, https://doi.org/10.1175/2008WAF2222159.1.

Rotunno, R., and J. B. Klemp, 1982: The influence of the shear-induced pressure gradient on thunderstorm motion. *Mon. Wea. Rev.*, **110**, 136–151, https://doi.org/10.1175/1520-0493(1982)110<0136:TIOTSI>2.0.CO;2.

——, and ——, 1985: On the rotation and propagation of simulated supercell thunderstorms. *J. Atmos. Sci.*, **42**, 271–292, https://doi.org/10.1175/1520-0469(1985)042<0271:OTRAPO>2.0.CO;2.

——, ——, and M. L. Weisman, 1988: A theory for strong, long-lived squall lines. *J. Atmos. Sci.*, **45**, 463–485, https://doi.org/10.1175/1520-0469(1988)045<0463:ATFSLL>2.0.CO;2.

Schaumann, J., and R. W. Przybylinski, 2012: Operational application of 0-3 km bulk shear vectors in assessing quasi linear convective system mesovortex and tornado potential. *26th Conf. on Severe Local Storms*, Nashville, TN, Amer. Meteor. Soc., 142, https://ams.confex.com/ams/26SLS/webprogram/Paper212008.html.

Shabbott, C. J., and P. M. Markowski, 2006: Surface in situ observations within the outflow of forward-flank downdrafts of supercell thunderstorms. *Mon. Wea. Rev.*, **134**, 1422–1441, https://doi.org/10.1175/MWR3131.1.

Shapiro, A., E. Fedorovich, and S. Rahimi, 2016: A unified theory for the Great Plains nocturnal low-level jet. *J. Atmos. Sci.*, **73**, 3037–3057, https://doi.org/10.1175/JAS-D-15-0307.1.

Sherburn, K. D., and M. D. Parker, 2014: Climatology and ingredients of significant severe convection in high-shear, low-CAPE environments. *Wea. Forecasting*, **29**, 854–877, https://doi.org/10.1175/WAF-D-13-00041.1.

——, and ——, 2019: The development of severe vortices within simulated high-shear, low-CAPE convection. *Mon. Wea. Rev.*, **147**, 2189–2216, https://doi.org/10.1175/MWR-D-18-0246.1.

——, ——, J. R. King, and G. M. Lackmann, 2016: Composite environments of severe and nonsevere high-shear, low-CAPE convective events. *Wea. Forecasting*, **31**, 1899–1927, https://doi.org/10.1175/WAF-D-16-0086.1.

Simmons, K. M., and D. Sutter, 2007: Tornado shelters and the housing market. *Construct. Manag. Econ.*, **25**, 1119–1126, https://doi.org/10.1080/01446190701618299.

Smith, B. T., R. L. Thompson, J. S. Grams, C. Broyles, and H. E. Brooks, 2012: Convective modes for significant severe thunderstorms in the contiguous United States. Part I: Storm classification and climatology. *Wea. Forecasting*, **27**, 1114–1135, https://doi.org/10.1175/WAF-D-11-00115.1.

Strader, S. M., W. S. Ashley, T. J. Pingel, and A. J. Krmenec, 2017: Observed and projected changes in U.S. tornado exposure. *Wea. Climate Soc.*, **9**, 109–123, https://doi.org/10.1175/WCAS-D-16-0041.1.

Thompson, R. L., R. Edwards, J. A. Hart, K. L. Elmore, and P. Markowski, 2003: Close proximity soundings within supercell environments obtained from the Rapid Update Cycle. *Wea. Forecasting*, **18**, 1243–1261, https://doi.org/10.1175/1520-0434(2003)018<1243:CPSWSE>2.0.CO;2.

——, B. T. Smith, J. S. Grams, A. R. Dean, and C. Broyles, 2012: Convective modes for significant severe thunderstorms in the contiguous United States. Part II: Supercell and QLCS tornado environments. *Wea. Forecasting*, **27**, 1136–1154, https://doi.org/10.1175/WAF-D-11-00116.1.

——, ——, A. R. Dean, and P. T. Marsh, 2013: Spatial distributions of tornadic near-storm environments by convective mode. *Electron. J. Severe Storms Meteor.*, **8** (5), https://ejssm.org/ojs/index.php/ejssm/article/viewArticle/125.

——, and Coauthors, 2017: Tornado damage rating probabilities derived from WSR-88D data. *Wea. Forecasting*, **32**, 1509–1528, https://doi.org/10.1175/WAF-D-17-0004.1.

Trapp, R. J., S. A. Tessendorf, E. S. Godfrey, and H. E. Brooks, 2005: Tornadoes from squall lines and bow echoes. Part I: Climatological distribution. *Wea. Forecasting*, **20**, 23–34, https://doi.org/10.1175/WAF-835.1.

Uccellini, L. W., and D. R. Johnson, 1979: The coupling of upper and lower tropospheric jet streaks and implications for the development of severe convective storms. *Mon. Wea. Rev.*, **107**, 682–703, https://doi.org/10.1175/1520-0493(1979)107<0682:TCOUAL>2.0.CO;2.

Wade, A. R., and M. D. Parker, 2021: Dynamics of simulated high-shear low-CAPE supercells. *J. Atmos. Sci.*, **78**, 1389–1410, https://doi.org/10.1175/JAS-D-20-0117.1.

Warren, R. A., H. Richter, H. A. Ramsay, S. T. Siems, and M. J. Manton, 2017: Impact of variations in upper-level shear on simulated supercells. *Mon. Wea. Rev.*, **145**, 2659–2681, https://doi.org/10.1175/MWR-D-16-0412.1.

Wilks, D. S., 2011: *Statistical Methods in the Atmospheric Sciences*. 3rd ed. International Geophysics Series, Vol. 100, Academic Press, 704 pp.

Williams, B. M., J. S. Allen, and J. W. Zeitler, 2018: Anticipating QLCS tornadogenesis for decision support: The three-ingredient method during the 19–20 February 2017 south-central Texas tornadic QLCS event. *Major Weather Events and Impacts of 2017*, Austin, TX, Amer. Meteor. Soc., 375, https://ams.confex.com/ams/98Annual/webprogram/Paper331351.html.

Ziegler, C. L., E. R. Mansell, J. M. Straka, D. R. MacGorman, and D. W. Burgess, 2010: The impact of spatial variations of low-level stability on the life cycle of a simulated supercell storm. *Mon. Wea. Rev.*, **138**, 1738–1766, https://doi.org/10.1175/2009MWR3010.1.